Measurement of the absolute branching fraction of the three-body decay $\Lambda_c^+ \to \Xi^0 K^+ \pi^0$ and search for $\Lambda_c^+ \to nK^+\pi^0$, $\Sigma^0 K^+ \pi^0$, and $\Lambda K^+ \pi^0$

M. Ablikim *et al.*[*]

(BESIII Collaboration)

The Cabbibo-favored decay $\Lambda_c^+ \to \Xi^0 K^+ \pi^0$ is studied for the first time using 6.1 fb^{-1} of e^+e^- collision data at center-of-mass energies between 4.600 and 4.840 GeV, collected with the BESIII detector at the BEPCII collider. With a double-tag method, the branching fraction of the three-body decay $\Lambda_c^+ \to \Xi^0 K^+ \pi^0$ is measured to be $(7.79 \pm 1.46 \pm 0.95) \times 10^{-3}$, where the first and second uncertainties are statistical and systematic, respectively. The branching fraction of the two-body decay $\Lambda_c^+ \to \Xi(1530)^0 K^+$ is $(5.99 \pm 1.04 \pm 0.32) \times 10^{-3}$, which is consistent with the previous result of $(5.02 \pm 0.99 \pm 0.31) \times 10^{-3}$. In addition, the upper limit on the branching fraction of the doubly Cabbibo-suppressed decay $\Lambda_c^+ \to nK^+\pi^0$ is 7.1×10^{-4} at the 90% confidence level. The upper limits on the branching fractions of $\Lambda_c^+ \to \Sigma^0 K^+ \pi^0$ and $\Lambda K^+ \pi^0$ are also determined to be 1.8×10^{-3} and 2.0×10^{-3}, respectively.

I. INTRODUCTION

Hadronic decays of charmed baryons provide an ideal laboratory to understand the interplay of weak and strong interactions in the charm system [1–9], and the measured branching fractions of charmed baryons play an important role in constraining models of charmed hadronic decays [10,11]. However, no reliable phenomenological model of charmed baryon decays currently exists. The Λ_c^+ baryon is the lightest charmed baryon, thus it is often a decay product in many charmed baryon decays. Hence, an investigation of the Λ_c^+ decay is essential for understanding excited charmed baryons [12]. In charmed baryon decays, the nonfactorizable contributions from W-exchange diagrams play an essential role. In contrast, these effects are negligible in heavy meson decays [13]. Therefore, measurements of the absolute branching fractions of Λ_c^+ decays are important to understanding the internal dynamics of charmed baryon decays [14].

In recent years, great progress has been made in the experimental study of the Λ_c^+ baryon at the Belle [15], LHCb [16] and BESIII experiments [17–20]. First, a breakthrough was achieved with the measurement of the

[*]Full author list given at the end of article.

absolute branching fraction of $\Lambda_c^+ \to pK^-\pi^+$ [21,22]. Next, BESIII directly measured the absolute branching fractions of twelve decay modes for the first time [21]. However, precise measurements for several Cabbibo-favored (CF) decays of Λ_c^+ are currently unavailable. Furthermore, a large number of the singly Cabbibo-suppressed (SCS) decays and the doubly Cabbibo-suppressed (DCS) decays of Λ_c^+ have not yet been studied. Based on the datasets at BESIII, measurements of the branching fractions of Λ_c^+ decays of currently known decay modes could potentially reach a sensitivity of 10^{-4}. In particular, the branching fraction of $\Lambda_c^+ \to n\pi^+$ was recently measured to be $(6.6 \pm 1.2 \pm 0.4) \times 10^{-4}$ [17]. In addition, the data allows for a search of many rare Λ_c^+ decays.

The three-body CF decay $\Lambda_c^+ \to \Xi^0 K^+ \pi^0$ is expected to have a large decay rate. Figure 1(a) presents a typical Feynman diagram of this decay. Some phenomenological models have predicted different branching fractions for the $\Lambda_c^+ \to \Xi^0 K^+ \pi^0$ decay, which are $(4.5 \pm 0.8) \times 10^{-2}$ [23] and $(3.2 \pm 0.6) \times 10^{-2}$ [24] by assuming SU(3) flavor symmetry and isospin asymmetry, respectively. Experimentally, there are only a few studies of Λ_c^+ decays with a Ξ^0 baryon in the final state, and the three-body decay $\Lambda_c^+ \to \Xi^0 K^+ \pi^0$ has not yet been studied. Measurement of the branching fraction will help us further understand the underlying dynamics of Λ_c^+ decays and distinguish among the different theoretical models [23].

The three-body DCS decay $\Lambda_c^+ \to nK^+\pi^0$ is also of great interest, and phenomenological models of this decay mode have been proposed [23,24]. SU(3) flavor symmetry
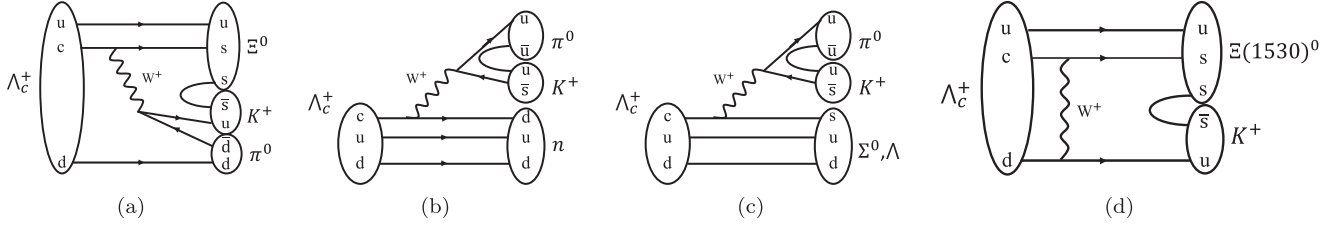
FIG. 1.   Typical Feynman diagrams of the decay (a) $\Lambda_c^+ \to \Xi^0 K^+ \pi^0$, (b) $nK^+\pi^0$, (c) $\Sigma^0(\Lambda)K^+\pi^0$ and (d) $\Xi(1530)^0 K^+$.

predicts the branching fraction of $\Lambda_c^+ \to nK^+\pi^0$ to be $(5.0 \pm 0.5) \times 10^{-5}$ [23]. Figure 1(b) shows a typical Feynman diagram of $\Lambda_c^+ \to nK^+\pi^0$. Experimental measurements of DCS decays of Λ_c^+ are limited due to the suppressed branching fractions. Currently, the only study of a DCS Λ_c^+ decay is $\Lambda_c^+ \to pK^+\pi^-$. The relative branching fraction $\mathcal{B}(\Lambda_c^+ \to pK^+\pi^-)/\mathcal{B}(\Lambda_c^+ \to pK^-\pi^+)$ is measured to be $(2.4 \pm 0.3 \pm 0.2) \times 10^{-3}$ [25].

In this paper, the three-body decays $\Lambda_c^+ \to \Xi^0 K^+\pi^0$, $\Lambda_c^+ \to nK^+\pi^0$, $\Lambda_c^+ \to \Sigma^0 K^+\pi^0$, $\Lambda_c^+ \to \Lambda K^+\pi^0$, and the two-body decay $\Lambda_c^+ \to \Xi(1530)^0 K^+$ are studied experimentally with a double-tag (DT) method [26]. Figure 1(c) and 1d show typical Feynman diagrams of $\Lambda_c^+ \to \Sigma^0(\Lambda)K^+\pi^0$ and $\Lambda_c^+ \to \Xi(1530)^0 K^+$, respectively. This analysis is performed using a data sample with an integrated luminosity of 6.1 fb^{-1} collected at center-of-mass (CM) energies between 4.600 and 4.840 GeV [27,28], listed in Table I, by the BESIII detector at the BEPCII collider. Throughout the text, the charge conjugate states are always implied.

II. BESIII DETECTOR AND MONTE CARLO

The BESIII detector [29] records symmetric e^+e^- collisions provided by the BEPCII [30] storage ring, which operates in the CM energy range from 2.0 to 4.95 GeV, with a peak luminosity of 1.1×10^{33} cm^{-2} s^{-1} achieved at

TABLE I.   The CM energy and the integrated luminosity ($\mathcal{L}_{\text{int}}$) for each energy point. The first and the second uncertainties are statistical and systematic, respectively.

Dataset	CM energy (MeV)	$\mathcal{L}_{\text{int}}$ (pb^{-1})
4.600	$4599.53 \pm 0.07 \pm 0.74$	$586.90 \pm 0.10 \pm 3.90$
4.612	$4611.84 \pm 0.12 \pm 0.28$	$103.45 \pm 0.05 \pm 0.64$
4.620	$4628.00 \pm 0.06 \pm 0.31$	$519.93 \pm 0.11 \pm 3.22$
4.640	$4640.67 \pm 0.06 \pm 0.36$	$548.15 \pm 0.12 \pm 3.40$
4.660	$4661.22 \pm 0.06 \pm 0.29$	$527.55 \pm 0.12 \pm 3.27$
4.680	$4681.84 \pm 0.08 \pm 0.29$	$1664.34 \pm 0.21 \pm 10.32$
4.700	$4698.57 \pm 0.10 \pm 0.32$	$534.40 \pm 0.12 \pm 3.31$
4.740	$4739.70 \pm 0.20 \pm 0.30$	$164.27 \pm 0.07 \pm 0.87$
4.750	$4750.05 \pm 0.12 \pm 0.29$	$367.21 \pm 0.10 \pm 1.95$
4.780	$4780.54 \pm 0.12 \pm 0.33$	$512.78 \pm 0.12 \pm 2.72$
4.840	$4843.07 \pm 0.20 \pm 0.31$	$527.29 \pm 0.12 \pm 2.79$

$\sqrt{s} = 3.77$ GeV [31]. The cylindrical core of the BESIII detector covers 93% of the full solid angle and consists of a helium-based multilayer drift chamber (MDC), a plastic scintillator time-of-flight system (TOF), and a CsI(Tl) electromagnetic calorimeter (EMC), which are all enclosed in a superconducting solenoidal magnet providing a 1.0 T magnetic field. The solenoid is supported by an octagonal flux-return yoke with resistive plate counter muon identification modules interleaved with steel [32]. The charged-particle momentum resolution at 1 GeV/c is 0.5%, and resolution of the ionization energy loss in the MDC (dE/dx) is 6% for electrons from Bhabha scattering. The EMC measures photon energies with a resolution of 2.5% (5%) at 1 GeV in the barrel (end cap) region. The time resolution in the TOF barrel region is 68 ps. The end-cap TOF system was upgraded in 2015 using multi-gap resistive plate chamber technology, providing a time resolution of 60 ps [33].

Simulated samples produced with GEANT4-based [34] Monte Carlo software, which includes the geometric description [35,36] of the BESIII detector and the detector response, are used to determine the detection efficiency and to estimate backgrounds. Exclusive simulation samples of $e^+e^- \to \Lambda_c^+\bar{\Lambda}_c^-$ are produced with $\bar{\Lambda}_c^-$ decaying into ten specific tag modes and Λ_c^+ decaying into $\Xi^0 K^+\pi^0$ and $nK^+\pi^0$. The resonances are modeled with Breit-Wigner functions, of which masses and widths are taken from the Particle Data Group (PDG) [37]. The simulation includes the beam-energy spread and initial-state radiation (ISR) in the e^+e^- annihilations with the specific tag modes [38] modeled with the generator KKMC [39,40]. The signal events are modeled with a phase-space generator. The $e^+e^- \to \Lambda_c^+\bar{\Lambda}_c^-$ line-shape implements the description from Ref. [18]. The inclusive simulation sample, which consists of $\Lambda_c^+\bar{\Lambda}_c^-$ events, $D_{(s)}$ production, ISR return to lower-mass ψ states, and continuum processes ($e^+e^- \to u\bar{u}$, $d\bar{d}$ and $s\bar{s}$) is used to estimate the potential background. All the known decay modes of charmed hadrons and charmonia are modeled with EVTGEN [41,42] using branching fractions either taken from the PDG [37], when available, or otherwise estimated with LUNDCHARM [43,44]. Final state radiation from charged final state particles is incorporated using PHOTOS [45].

III. METHODOLOGY

The $\bar{\Lambda}_c^-$ baryons are fully reconstructed by their hadronic decays to $\bar{p}K^+\pi^-$, $\bar{p}K_S^0$, $\bar{p}K^+\pi^-\pi^0$, $\bar{p}K_S^0\pi^0$, $\bar{p}K_S^0\pi^+\pi^-$, $\bar{\Lambda}\pi^-$, $\bar{\Lambda}\pi^-\pi^-\pi^+$, $\bar{\Lambda}\pi^-\pi^0$, $\bar{\Sigma}^0\pi^-$ and $\bar{\Sigma}^-\pi^+\pi^-$. These reconstructed decays are referred to as single-tag (ST) $\bar{\Lambda}_c^-$ baryons, where the intermediate particles K_S^0, $\bar{\Lambda}$, $\bar{\Sigma}^0$, $\bar{\Sigma}^-$, and π^0 are reconstructed via $K_S^0 \to \pi^+\pi^-$, $\bar{\Lambda} \to \bar{p}\pi^+$, $\bar{\Sigma}^0 \to \gamma\bar{\Lambda}$, $\bar{\Sigma}^- \to \bar{p}\pi^0$ and $\pi^0 \to \gamma\gamma$, respectively. From the remaining tracks and showers, the three-body decays $\Lambda_c^+ \to \Xi^0 K^+\pi^0$, $nK^+\pi^0$, $\Sigma^0 K^+\pi^0$ and $\Lambda K^+\pi^0$ are selected to form Λ_c^+ candidates, which will be referred to as the recoiling system. Together with the $\bar{\Lambda}_c^-$ candidates, these form a sample of DT events.

The branching fraction is expressed as:

$$\mathcal{B} = \frac{N_{\mathrm{sig}}}{\mathcal{B}_{\mathrm{inter}} \cdot \Sigma_i N_i^{\mathrm{ST}} \cdot (\epsilon_i^{\mathrm{DT}}/\epsilon_i^{\mathrm{ST}})}, \qquad (1)$$

where N_{sig} is the signal yield of the DT candidates and $\mathcal{B}_{\mathrm{inter}}$ is the product of branching fractions of intermediate decays on the signal side from the PDG [37]. N_i^{ST} denotes the yields of the ST candidates observed in data, and ϵ_i^{ST} and ϵ_i^{DT} are the ST and DT efficiencies, respectively.

IV. EVENT SELECTION

The selection criteria in this analysis follow that of Ref. [17]. Charged tracks are required to have a polar angle (θ) within $|\cos\theta| < 0.93$, where θ is defined with respect to the z-axis, which is the symmetry axis of the MDC. Tracks, except for those from K_S^0 and $\bar{\Lambda}$ decays, are required to originate from an interaction region defined by $|V_{xy}| < 1$ cm and $|V_z| < 10$ cm (referred as a tight track hereafter), where $|V_{xy}|$ and $|V_z|$ refer to the distances of closest approach of the reconstructed track to the interaction point (IP) in the xy plane and the z direction, respectively.

Particle identification (PID) for charged tracks combines measurements of the energy deposited in the MDC (dE/dx) and the flight time in the TOF to form likelihoods $\mathcal{L}(h)(h = p, K, \pi)$ for each hadron h hypothesis. Tracks are identified as protons when the proton hypothesis has the greatest likelihood $[\mathcal{L}(p) > \mathcal{L}(K)$ and $\mathcal{L}(p) > \mathcal{L}(\pi)]$, while charged kaons and pions are identified by comparing the likelihoods for the kaon and pion hypotheses, $\mathcal{L}(K) > \mathcal{L}(\pi)$ and $\mathcal{L}(\pi) > \mathcal{L}(K)$, respectively.

The selection of tracks from K_S^0 and $\bar{\Lambda}$ is different from those of other tracks. Candidates of K_S^0 and $\bar{\Lambda}$ hadrons are reconstructed from their decays to $\pi^+\pi^-$ and $\bar{p}\pi^+$, respectively, where the charged tracks must satisfy $|V_z| < 20$ cm (referred as a loose track hereafter). The PID selection criteria are imposed on the antiproton candidate, while the charged pion is not subject to any PID requirement. A secondary vertex fit is performed for each K_S^0 or $\bar{\Lambda}$

candidate, and the momentum obtained from the fit is used in the subsequent analysis. The K_S^0 or $\bar{\Lambda}$ candidate is retained if the χ^2 of the secondary vertex fit is less than 100. Furthermore, the decay vertex is required to be separated from the IP by a distance of at least twice the vertex resolution. For K_S^0 and $\bar{\Lambda}$, the invariant masses of $\pi^+\pi^-$ and $\bar{p}\pi^+$ pairs are required to be within (0.487, 0.511) GeV/c^2 and (1.111, 1.121) GeV/c^2, respectively. The $\pi^+\pi^-$ and $\bar{p}\pi^-$ invariant mass resolutions determined through simulations, are 2.9 MeV/c^2 and 1.2 MeV/c^2, respectively. Similarly, the $\bar{\Sigma}^0$ and $\bar{\Sigma}^-$ candidates are reconstructed from the $\gamma\bar{\Lambda}$ and $\bar{p}\pi^0$ final states with invariant masses within the ranges of (1.179, 1.203) GeV/c^2 and (1.176, 1.200) GeV/c^2, respectively. The mass resolutions for $\bar{\Sigma}^0$ and $\bar{\Sigma}^-$ are found, using simulation, to be 3.6 MeV/c^2 and 4.3 MeV/c^2, respectively.

Photon candidates are identified using showers in the EMC. The deposited energy of each shower must be more than 25 MeV in the barrel region ($|\cos\theta| \leq 0.80$) or more than 50 MeV in the end cap region ($0.86 \leq |\cos\theta| \leq 0.92$). To suppress electronic noise and showers unrelated to the event, the difference between the EMC time and the event start time is required to be within (0, 700) ns.

A π^0 candidate is reconstructed with a photon pair, and their invariant mass is required to be within the range (0.115, 0.150) GeV/c^2. To improve the resolution, a kinematic fit is performed, where the diphoton invariant mass is constrained to the known π^0 mass [37], and the χ^2 of the kinematic fit is required to be less than 200. The momenta obtained from the kinematic fit are used in the subsequent analysis.

To distinguish the ST $\bar{\Lambda}_c^-$ baryons from combinatorial backgrounds, the distributions of the energy difference ΔE are used, defined as

$$\Delta E \equiv E_{\bar{\Lambda}_c^-} - E_{\mathrm{beam}}, \qquad (2)$$

where E_{beam} is the beam energy, and $E_{\bar{\Lambda}_c^-}$ is the total energy of the ST candidate, calculated in the e^+e^- rest frame. The signal events are expected to peak around zero in the ΔE distribution. If an event has multiple $\bar{\Lambda}_c^-$ candidates, the one with the smallest $|\Delta E|$ is retained, and the ΔE requirements are listed in Table II.

The beam-constrained mass M_{BC} of the selected ST candidates is defined as

$$M_{\mathrm{BC}} \equiv \sqrt{E_{\mathrm{beam}}^2/c^4 - |\vec{p}_{\bar{\Lambda}_c^-}|^2/c^2}, \qquad (3)$$

where $\vec{p}_{\bar{\Lambda}_c^-}$ is the total momentum of the ST candidate and M_{BC} peaks at the $\bar{\Lambda}_c^-$ mass. For each tag mode, the ST yield is determined by fitting the M_{BC} distribution. In the fit, the $\bar{\Lambda}_c^-$ signal is described by the MC simulated shape

TABLE II.   The ΔE requirements, the ST yields, and the ST detection efficiencies of each tag mode for the data samples between 4.740 and 4.840 GeV. The uncertainties of the ST yields are statistical only.

Tag mode	ΔE (MeV)	4.740 N_i^{ST}	ϵ_i^{ST} (%)	4.750 N_i^{ST}	ϵ_i^{ST} (%)	4.780 N_i^{ST}	ϵ_i^{ST} (%)	4.840 N_i^{ST}	ϵ_i^{ST} (%)
$\bar{p}K^+\pi^-$	$(-34, 20)$	1201 ± 40	48.4	2782 ± 60	48.1	3689 ± 67	47.1	2676 ± 61	43.8
$\bar{p}K_S$	$(-20, 20)$	256 ± 17	48.5	525 ± 24	46.9	629 ± 26	44.2	475 ± 23	42.4
$\bar{\Lambda}\pi^-$	$(-20, 20)$	144 ± 12	36.6	336 ± 19	37.0	383 ± 21	35.5	265 ± 17	32.8
$\bar{p}K^+\pi^-\pi^0$	$(-30, 20)$	246 ± 25	17.8	607 ± 40	18.3	845 ± 37	17.3	583 ± 39	15.7
$\bar{p}K_S\pi^0$	$(-30, 20)$	76 ± 12	18.7	212 ± 20	18.8	269 ± 22	18.3	185 ± 20	10.9
$\bar{\Lambda}\pi^-\pi^0$	$(-30, 20)$	239 ± 18	18.1	529 ± 30	17.8	723 ± 33	18.0	513 ± 28	16.9
$\bar{p}K_S\pi^+\pi^-$	$(-20, 20)$	89 ± 13	20.1	192 ± 20	19.3	292 ± 24	19.7	202 ± 20	17.6
$\bar{\Lambda}\pi^-\pi^+\pi^-$	$(-20, 20)$	152 ± 14	13.6	326 ± 21	14.7	453 ± 25	17.5	348 ± 22	13.2
$\bar{\Sigma}^0\pi^-$	$(-20, 20)$	58 ± 8	22.5	152 ± 13	22.0	196 ± 15	20.9	145 ± 13	20.5
$\bar{\Sigma}^-\pi^+\pi^-$	$(-30, 20)$	136 ± 16	19.9	362 ± 32	19.6	500 ± 32	19.9	373 ± 26	17.5

convolved with a Gaussian function to compensate for the resolution difference between data and MC. The parameters of the Gaussian function are free in the fit and different for each energy and tag mode. The combinatorial background is described by an ARGUS function [46], with the endpoint parameter fixed to the nominal beam energy. The fits to the M_{BC} distributions of the various tag modes for the 4.600–4.700 datasets are the same as Ref. [38]. The fits to the M_{BC} distributions for the 4.740, 4.750, 4.780, and 4.840 datasets are shown in Fig. 2. Candidates in the M_{BC} signal region, $(2.275, 2.310)$ GeV/c^2, are kept for further analysis. The ST yields in data and the ST efficiencies for individual tags are listed in Table II. The total ST yield, obtained by summing the ST yield of all tag modes and all energies, is found to be $N_{\mathrm{ST}}^{\mathrm{tot}} = 130439 \pm 425$, where the uncertainty is statistical.

After the ST selection, we want to determine the number of $\Lambda_c^+ \to \Xi^0 K^+\pi^0$, $nK^+\pi^0$, $\Sigma^0 K^+\pi^0$ and $\Lambda K^+\pi^0$ candidates on the opposite side of the ST $\bar{\Lambda}_c^-$. The K^+ and π^0 are reconstructed, as described above, from the remaining showers and tracks. Using total four-momentum conservation, the Ξ^0 signal is obtained from the distribution of recoil mass,

$$M_{\mathrm{recoil}}^2(\Lambda_c^{\mathrm{ST}}K^+\pi^0) = (E_{\mathrm{beam}} - E_{K^+} - E_{\pi^0})^2/c^4$$
$$- |\rho \cdot \vec{p}_0 - \vec{p}_{K^+} - \vec{p}_{\pi^0}|^2/c^2, \quad (4)$$

where E_{K^+}, E_{π^0}, $\vec{p}_{K^+}$, and $\vec{p}_{\pi^0}$ are the energies and momenta of K^+ and π^0 candidates, respectively, $\rho = \sqrt{E_{\mathrm{beam}}^2/c^2 - m_{\Lambda_c^+}^2 c^2}$ is the magnitude of the Λ_c^+ momentum, constrained by the beam energy, and $\vec{p}_0 = -\vec{p}_{\bar{\Lambda}_c^-}/|\vec{p}_{\bar{\Lambda}_c^-}|$ is its direction. Similarly, the yield of the two-body decay $\Lambda_c^+ \to \Xi(1530)^0 K^+$ is obtained using the recoil mass.

$$M_{\mathrm{recoil}}^2(\Lambda_c^{\mathrm{ST}}K^+) = (E_{\mathrm{beam}} - E_{K^+})^2/c^4 - |\rho \cdot \vec{p}_0 - \vec{p}_{K^+}|^2/c^2.$$
$$(5)$$

The $\Xi(1530)^0$, Ξ^0 and Σ^0 predominant decay modes are $\Xi(1530)^0 \to \Xi\pi$, $\Xi^0 \to \Lambda\pi^0$ and $\Sigma^0 \to \Lambda\gamma$ [37], respectively. The Λ baryon has two main decay modes, which are studied in this analysis: the neutral decay mode $\Lambda \to n\pi^0$, which will be referred to as Cat-1, and the charged decay mode $\Lambda \to p\pi^-$, which will be referred to as Cat-2. The Cat-1 and Cat-2 decays are shown schematically in Fig. 3. Four variables $M_{\mathrm{recoil}}^{\mathrm{Cat}-1}(\Lambda_c^{\mathrm{ST}}K^+\pi^0)$, $M_{\mathrm{recoil}}^{\mathrm{Cat}-2}(\Lambda_c^{\mathrm{ST}}K^+\pi^0)$, $M_{\mathrm{recoil}}^{\mathrm{Cat}-1}(\Lambda_c^{\mathrm{ST}}K^+)$ and $M_{\mathrm{recoil}}^{\mathrm{Cat}-2}(\Lambda_c^{\mathrm{ST}}K^+)$ are defined by Eqs. (4) and (5). For Cat-1, a single tight track is reconstructed and identified as a K^+ meson. In Cat-2, three charged tracks are reconstructed as a K^+, p, and π^-. The K^+ is a tight track, while the other two are loose tracks from the $\Lambda \to p\pi^-$ decay. The p and π^- are constrained to originate from a common vertex to form the Λ candidates by a vertex fit [47]. The invariant mass of the Λ candidate is required to fall inside the range $(1.111, 1.121)$ GeV/c^2.

The π^0 candidate is reconstructed via the process $\pi^0 \to \gamma\gamma$. If there are multiple π^0 candidates, the one with the minimum kinematic-fit χ^2 is assumed to originate from the Λ_c^+ baryon.

To suppress sources of background due to neutral hyperon decays from the decays $\Lambda_c^+ \to \Lambda K^+$, $\Sigma^0 K^+$ and $\Xi^0 K^+$, the events falling inside the corresponding intervals of these three decays of the variable $M_{\mathrm{recoil}}^{\mathrm{Cat}-1}(\Lambda_c^{\mathrm{ST}}K^+)$ are rejected. This requirement suppresses 95% of these backgrounds. Furthermore, electron mis-PID backgrounds are suppressed using PID and EMC information. To suppress contaminations from long-lived particles in the final state, any event with additional tracks, either loose or tight, is rejected. The DT efficiencies of each signal decay for Cat-1 and Cat-2 are summarized in Tables III–VII.
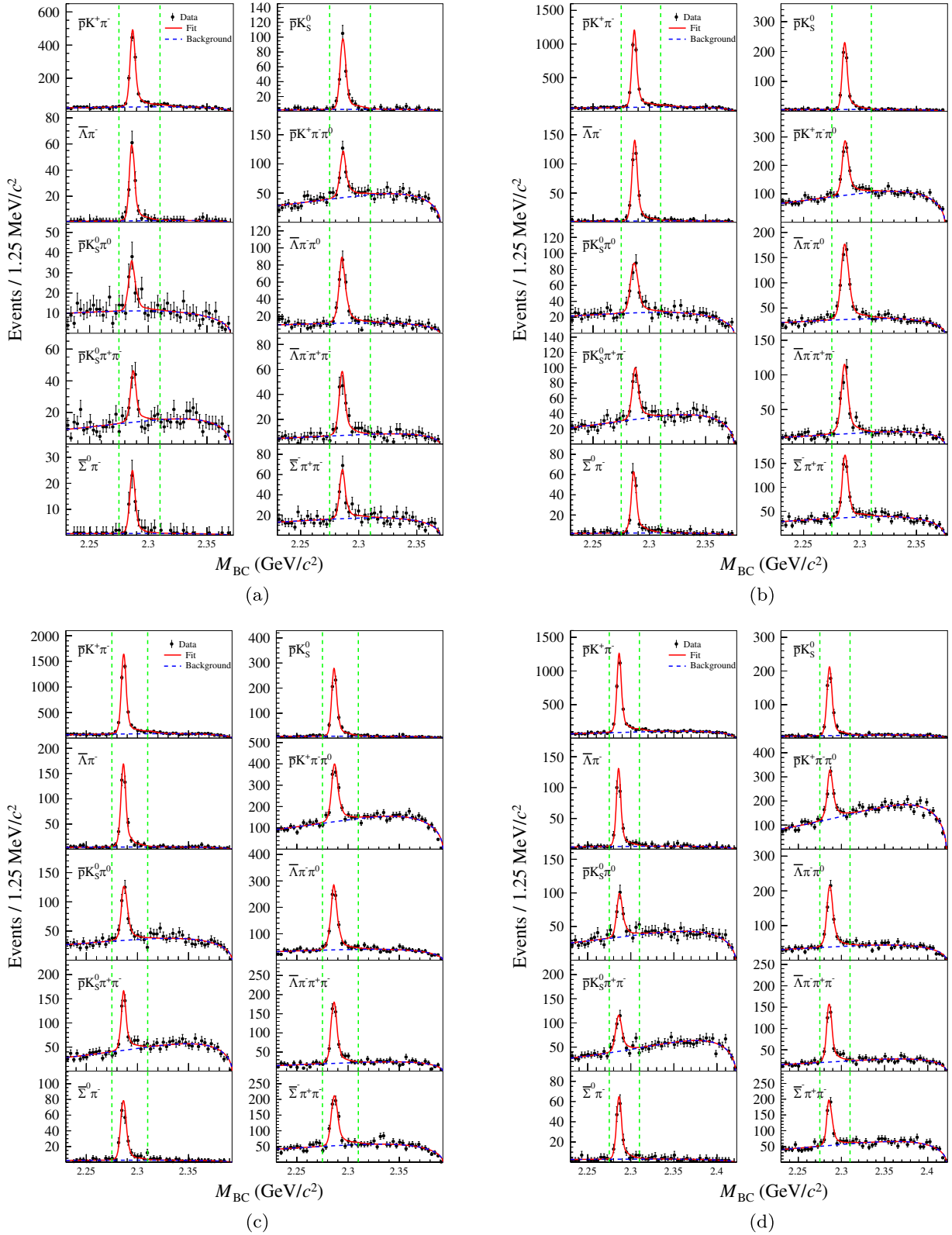
FIG. 2. The M_{BC} distributions of ST channels of $\bar{\Lambda}_c^-$ at (a) 4.740 GeV, (b) 4.750 GeV, (c) 4.780 GeV and (d) 4.840 GeV. The signal shape of the $\bar{\Lambda}_c^-$ is described by the simulated shape convolved with a Gaussian resolution function, and the background is modeled with an ARGUS function. The points with error bars represent data. The (red) solid curves indicate the fit results and the (blue) dashed curves describe the background shapes. The vertical dashed lines show the M_{BC} selection requirements.
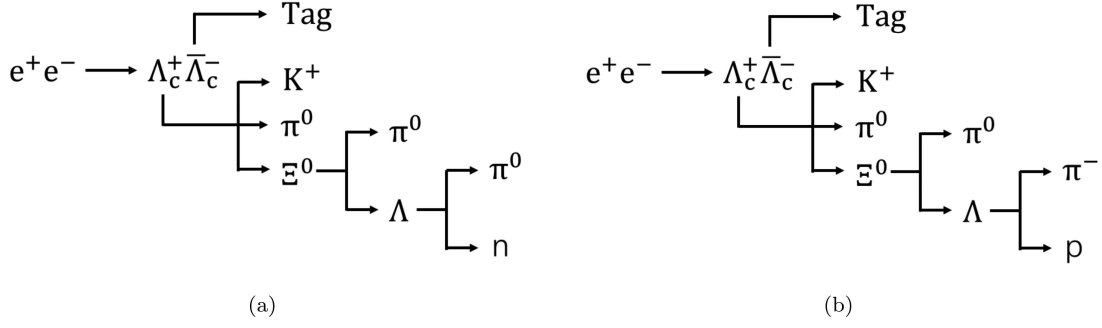
FIG. 3.   The schematic diagrams of the two analysis strategies, which are denoted (a) Cat-1 and (b) Cat-2 in the text.

TABLE III.   The DT detection efficiency(%) of $\Lambda_c^+ \to \Xi(1530)^0 K^+$ in Cat-1/Cat-2 for each tag mode and each energy point.

	4.600	4.612	4.620	4.640	4.660	4.680	4.700	4.740	4.750	4.780	4.840
$pK^-\pi^+$	20.3/8.3	19.3/7.4	19.0/6.7	18.6/6.7	18.1/6.5	17.8/6.5	17.4/6.5	15.7/6.5	15.4/6.4	14.9/6.5	13.8/6.1
pK_S^0	22.1/9.0	20.4/7.6	18.7/8.0	18.9/8.1	18.4/6.7	17.4/8.2	17.5/7.5	17.3/7.1	16.8/7.1	17.0/6.6	14.0/6.6
$\Lambda\pi^+$	16.9/7.9	15.6/6.9	14.5/6.2	14.5/6.0	13.3/6.1	13.0/5.6	13.6/4.9	13.9/5.3	13.4/5.4	12.1/5.1	12.1/4.6
$pK^-\pi^+\pi^0$	5.3/1.6	4.8/1.4	4.6/1.5	4.5/1.3	4.4/1.3	4.3/1.3	4.1/1.3	3.6/1.4	3.5/1.4	3.5/1.5	3.3/1.4
$pK_S^0\pi^0$	8.0/2.9	7.1/2.3	7.1/2.0	6.8/2.1	6.5/2.2	6.6/2.5	6.0/2.1	5.6/2.1	5.3/2.2	5.1/2.1	4.8/2.0
$\Lambda\pi^+\pi^0$	6.7/2.0	6.0/1.7	5.8/1.8	5.7/1.8	5.4/1.6	5.2/1.7	5.1/1.7	4.5/1.8	4.7/1.7	4.4/1.7	4.1/1.8
$pK_S^0\pi^+\pi^-$	9.0/2.9	8.7/2.4	8.1/2.0	7.9/2.2	7.9/2.2	7.4/2.2	7.4/2.6	6.7/2.5	7.0/2.7	6.7/2.8	6.1/2.5
$\Lambda\pi^+\pi^+\pi^-$	6.2/1.7	5.7/1.3	5.4/1.6	5.3/1.3	5.1/1.4	5.3/1.4	5.2/1.4	4.7/1.6	4.5/1.7	4.2/1.6	4.4/1.8
$\Sigma^0\pi^+$	8.8/3.7	7.8/3.0	7.8/2.4	7.3/2.8	6.4/2.4	6.6/3.4	6.9/2.6	5.8/2.5	6.0/2.3	5.4/2.4	5.0/2.3
$\Sigma^+\pi^+\pi^-$	3.2/2.5	3.2/2.3	3.0/2.3	3.0/2.4	2.6/2.0	2.8/1.9	2.7/2.2	2.3/1.0	2.4/1.0	2.2/1.1	2.0/0.8

TABLE IV.   The DT detection efficiency(%) of $\Lambda_c^+ \to \Xi^0 K^+ \pi^0$ in Cat-1/Cat-2 for each tag mode and each energy point.

	4.600	4.612	4.620	4.640	4.660	4.680	4.700	4.740	4.750	4.780	4.840
$pK^-\pi^+$	7.7/3.3	7.4/2.8	7.3/2.8	7.2/2.7	7.0/2.6	7.1/2.7	6.8/2.8	6.3/2.6	6.3/2.8	5.9/2.8	5.7/2.4
pK_S^0	8.6/3.7	8.5/3.2	7.6/3.1	7.7/2.8	7.7/2.9	7.7/3.2	7.3/2.5	6.5/3.3	6.7/2.9	6.6/3.2	6.3/2.4
$\Lambda\pi^+$	6.3/2.4	6.0/2.0	6.1/2.2	6.1/2.1	5.1/2.1	5.5/1.9	5.9/2.4	5.3/2.2	5.5/2.3	5.2/2.5	4.7/2.1
$pK^-\pi^+\pi^0$	1.9/0.8	2.0/0.7	2.0/0.7	1.9/0.6	2.0/0.6	1.8/0.7	1.8/0.6	1.5/0.6	1.4/0.6	1.5/0.6	1.3/0.6
$pK_S^0\pi^0$	2.9/1.1	2.5/1.1	2.5/1.0	2.3/1.0	2.5/1.1	2.6/0.9	2.4/1.0	2.1/0.7	2.1/0.8	2.0/0.9	2.2/0.8
$\Lambda\pi^+\pi^0$	2.5/0.9	2.2/0.8	2.1/0.8	2.1/0.8	2.1/0.7	2.0/0.8	2.0/0.8	1.8/0.7	1.7/0.7	1.9/0.8	1.8/0.7
$pK_S^0\pi^+\pi^-$	3.2/1.4	2.7/1.0	3.0/1.0	3.1/1.0	2.6/1.1	2.7/0.9	3.0/1.1	2.4/0.9	2.8/1.0	2.7/1.0	2.5/1.1
$\Lambda\pi^+\pi^+\pi^-$	2.2/0.8	2.0/0.6	1.8/0.6.	2.0/0.6	1.9/0.6	1.9/0.6	1.9/0.7	1.8/0.7	1.6/0.6	1.6/0.6	1.8/0.6
$\Sigma^0\pi^+$	3.2/1.3	2.8/1.3	2.9/1.1	2.5/1.3	2.8/1.3	2.9/1.1	2.5/1.0	2.7/1.1	2.4/1.2	2.2/1.0	2.2/1.0
$\Sigma^+\pi^+\pi^-$	1.3/0.7	1.2/0.4	1.1/0.4.	1.1/0.5	1.1/0.4	1.0/0.5	1.0/0.4	0.8/0.5	0.8/0.4	0.8/0.4	0.9/0.3

TABLE V.   The DT detection efficiency(%) of $\Lambda_c^+ \to n K^+ \pi^0$ in Cat-1 for each tag mode and each energy point.

	4.600	4.612	4.620	4.640	4.660	4.680	4.700	4.740	4.750	4.780	4.840
$pK^-\pi^+$	13.4	12.9	12.2	12.0	11.7	11.4	11.2	10.4	10.2	9.9	9.2
pK_S^0	14.3	13.8	13.3	12.9	12.1	12.5	11.5	11.2	11.6	11.1	9.9
$\Lambda\pi^+$	11.3	10.6	9.7	10.0	9.3	9.4	9.5	9.3	8.2	7.9	8.1
$pK^-\pi^+\pi^0$	3.7	3.6	3.5	3.3	3.3	3.2	3.2	2.7	2.7	2.8	2.5
$pK_S^0\pi^0$	4.8	4.5	4.3	4.5	4.2	4.0	3.8	3.1	3.4	3.4	3.0
$\Lambda\pi^+\pi^0$	4.2	4.0	3.6	3.7	3.5	3.4	3.4	3.2	3.1	3.0	2.7
$pK_S^0\pi^+\pi^-$	5.8	5.2	4.8	4.9	4.6	4.5	4.8	4.3	3.8	4.3	4.2
$\Lambda\pi^+\pi^+\pi^-$	3.9	3.3	3.5	3.2	3.4	3.4	2.9	2.7	2.8	2.7	2.8
$\Sigma^0\pi^+$	6.7	5.8	6.2	5.5	5.2	5.5	6.0	4.3	5.0	4.0	4.1
$\Sigma^+\pi^+\pi^-$	2.4	2.3	2.1	2.3	2.2	2.2	2.0	1.8	1.9	1.9	1.6

TABLE VI. The DT detection efficiency(%) of $\Lambda_c^+ \to \Sigma^0 K^+ \pi^0$ in Cat-1/Cat-2 for each tag mode and each energy point.

	4.600	4.612	4.620	4.640	4.660	4.680	4.700	4.740	4.750	4.780	4.840
$pK^-\pi^+$	10.2/5.7	9.7/5.3	9.0/4.9	9.3/4.9	9.2/4.9	8.7/4.8	8.6/4.7	8.3/4.5	8.1/4.6	7.7/4.5	7.5/4.2
pK_S^0	11.4/6.1	10.0/5.5	9.7/5.3	9.9/5.6	10.0/5.5	9.0/5.0	9.4/4.6	8.8/5.5	8.6/5.4	8.5/4.9	8.2/4.8
$\Lambda\pi^+$	8.5/4.8	8.5/3.6	7.3/3.9	7.4/4.3	7.7/3.9	7.0/4.0	6.8/3.3	6.9/3.9	6.9/4.2	6.2/3.7	6.0/3.5
$pK^-\pi^+\pi^0$	2.7/1.2	2.4/1.1	2.5/1.1	2.4/1.1	2.3/1.1	2.2/0.9	2.4/1.0	2.0/0.9	2.0/1.0	1.9/1.0	1.9/1.0
$pK_S^0\pi^0$	4.1/1.7	3.3/2.0	3.4/1.7	3.2/1.8	3.0/1.7	3.4/1.6	3.1/1.8	3.3/1.5	2.7/1.4	2.7/1.7	2.4/1.3
$\Lambda\pi^+\pi^0$	3.1/1.7	2.9/1.3	2.7/1.4	2.8/1.4	2.8/1.2	2.8/1.3	2.5/1.2	2.3/1.3	2.3/1.3	2.4/1.2	2.1/1.2
$pK_S^0\pi^+\pi^-$	4.5/2.1	4.1/1.8	3.6/1.9	3.8/1.9	3.8/1.5	3.4/1.7	3.8/1.7	3.7/1.6	3.0/1.5	3.5/1.6	3.4/1.8
$\Lambda\pi^+\pi^+\pi^-$	3.1/1.4	2.6/1.2	2.5/1.1	2.7/1.2	2.7/1.3	2.5/1.1	2.5/1.2	2.2/1.1	2.2/1.2	2.2/1.2	2.2/1.2
$\Sigma^0\pi^+$	4.4/2.1	4.6/2.1	3.7/2.2	3.6/1.9	3.9/1.6	3.8/1.8	3.6/1.9	3.4/2.0	3.5/1.7	3.2/1.7	3.1/1.7
$\Sigma^+\pi^+\pi^-$	1.8/1.0	1.6/0.8	1.5/0.8	1.5/0.8	1.5/0.8	1.4/0.9	1.6/0.7	1.2/0.7	1.2/0.7	1.3/0.8	1.2/0.8

TABLE VII. The DT detection efficiency(%) of $\Lambda_c^+ \to \Lambda K^+ \pi^0$ in Cat-1/Cat-2 for each tag mode and each energy point.

	4.600	4.612	4.620	4.640	4.660	4.680	4.700	4.740	4.750	4.780	4.840
$pK^-\pi^+$	11.0/6.4	10.5/6.0	10.0/5.6	10.0/5.4	10.1/5.4	9.9/5.5	9.5/5.4	8.7/5.0	8.6/5.1	8.2/5.0	7.9/4.6
pK_S^0	11.9/7.2	10.9/6.7	10.9/6.2	11.1/6.1	10.5/6.0	9.9/5.6	9.6/5.6	9.6/5.8	9.4/5.9	9.3/5.9	8.5/5.3
$\Lambda\pi^+$	9.8/4.9	9.0/4.8	7.9/4.5	8.6/5.0	8.0/4.5	7.1/4.6	7.8/4.3	7.6/4.3	7.3/4.8	8.2/4.3	7.4/3.7
$pK^-\pi^+\pi^0$	3.0/1.4	2.9/1.3	2.8/1.3	2.8/1.2	2.6/1.2	2.6/1.2	2.7/1.1	2.3/1.2	2.2/1.2	2.2/1.1	2.1/1.1
$pK_S^0\pi^0$	4.6/2.3	3.6/1.9	3.9/1.7	3.5/1.8	3.2/1.8	3.4/1.9	3.5/1.5	2.7/1.7	3.2/1.6	2.9/1.6	2.5/1.6
$\Lambda\pi^+\pi^0$	3.5/1.9	3.2/1.7	3.1/1.6	3.1/1.6	3.1/1.5	3.0/1.5	2.7/1.5	2.6/1.4	2.4/1.3	2.4/1.3	2.3/1.3
$pK_S^0\pi^+\pi^-$	4.7/2.4	4.1/2.1	4.0/1.9	4.4/1.9	4.2/1.8	3.8/2.0	4.1/1.8	3.8/2.0	3.4/2.0	4.1/2.1	3.5/1.9
$\Lambda\pi^+\pi^+\pi^-$	3.0/1.7	2.7/1.3	2.7/1.4	2.7/1.4	2.7/1.3	2.8/1.4	2.9/1.4	2.4/1.4	2.8/1.3	2.5/1.3	2.3/1.4
$\Sigma^0\pi^+$	5.1/2.8	4.5/2.4	4.4/2.7	4.6/2.4	4.2/2.4	4.4/2.1	4.0/2.2	3.8/2.6	3.4/2.5	3.3/2.2	3.0/2.1
$\Sigma^+\pi^+\pi^-$	2.1/1.4	1.9/1.1	1.8/1.1	1.6/1.0	1.8/1.1	1.6/1.0	1.5/0.9	1.6/0.8	1.5/0.9	1.3/0.8	1.3/0.8

V. BACKGROUND ANALYSIS

Potential sources of background are classified intotwo categories: those from $e^+e^- \to \Lambda_c^+\bar{\Lambda}_c^-$ (denoted as $\Lambda_c^+\bar{\Lambda}_c^-$ background) and those directly originating from continuum hadron production in e^+e^- annihilation (denoted as $q\bar{q}$ background).

The $\Lambda_c^+\bar{\Lambda}_c^-$ background is investigated for both categories with the $\Lambda_c^+\bar{\Lambda}_c^-$ inclusive MC samples, after removing the signal processes. The $\Lambda_c^+\bar{\Lambda}_c^-$ background distributions are the blue-shaded histograms in Figs. 4 and 5, and they have been normalized to the same luminosity as data.

For the Cat-1 $q\bar{q}$ background, the data events in the M_{BC} sideband region, defined as $M_{\mathrm{BC}} \in (2.200, 2.265)$ GeV/c^2, are used. Since $\Lambda_c^+\bar{\Lambda}_c^-$ background is present in the sideband region, it is estimated using inclusive simulation samples and subtracted from the total sideband yield to determine the $q\bar{q}$ background in the sideband. The $q\bar{q}$ background in the signal region is extrapolated from the yield in the sideband using information from the simulation. In Cat-2, the simulated $q\bar{q}$ samples are used.

There exists a contamination from mismatched π^0 candidates (denoted as π^0 mismatch), which consists of three sources: the first is due to the selection of an incorrect π^0 candidate in a signal event with multiple π^0 candidates; the second is where the π^0 candidate is reconstructed using photons that originated from two different π^0 decays; the third is caused by noise in the EMC, which creates a fake photon candidate that is used in the π^0 reconstruction. It has a wide shape and will not contribute to the narrow resonances in the distributions of $M_{\mathrm{recoil}}^{\mathrm{Cat-1}}(\Lambda_c^{\mathrm{ST}}K^+\pi^0)$ and $M_{\mathrm{recoil}}^{\mathrm{Cat-2}}(\Lambda_c^{\mathrm{ST}}K^+\pi^0)$. The π^0 mismatch background is estimated using simulation samples. Events containing showers where the angular separation between the true and reconstructed π^0 directions is greater than 20° are considered π^0 mismatch background, and the background is normalized according to the branching fractions of $\Lambda_c^+ \to \Xi(1530)^0 K^+$ and $\Lambda_c^+ \to \Xi^0 K^+ \pi^0$ in the distributions of $M_{\mathrm{recoil}}^{\mathrm{Cat-1}}(\Lambda_c^{\mathrm{ST}}K^+\pi^0)$ and $M_{\mathrm{recoil}}^{\mathrm{Cat-2}}(\Lambda_c^{\mathrm{ST}}K^+\pi^0)$.

VI. BRANCHING FRACTION MEASUREMENT

For the two-body decay $\Lambda_c^+ \to \Xi(1530)^0 K^+$, a simultaneous fit is performed by combining the Cat-1 and Cat-2 distributions of $M_{\mathrm{recoil}}^{\mathrm{Cat-1}}(\Lambda_c^{\mathrm{ST}}K^+)$ and $M_{\mathrm{recoil}}^{\mathrm{Cat-2}}(\Lambda_c^{\mathrm{ST}}K^+)$. The signal shapes are modeled with the simulation shapes convolved with a Gaussian function representing the resolution difference between data and simulation samples.
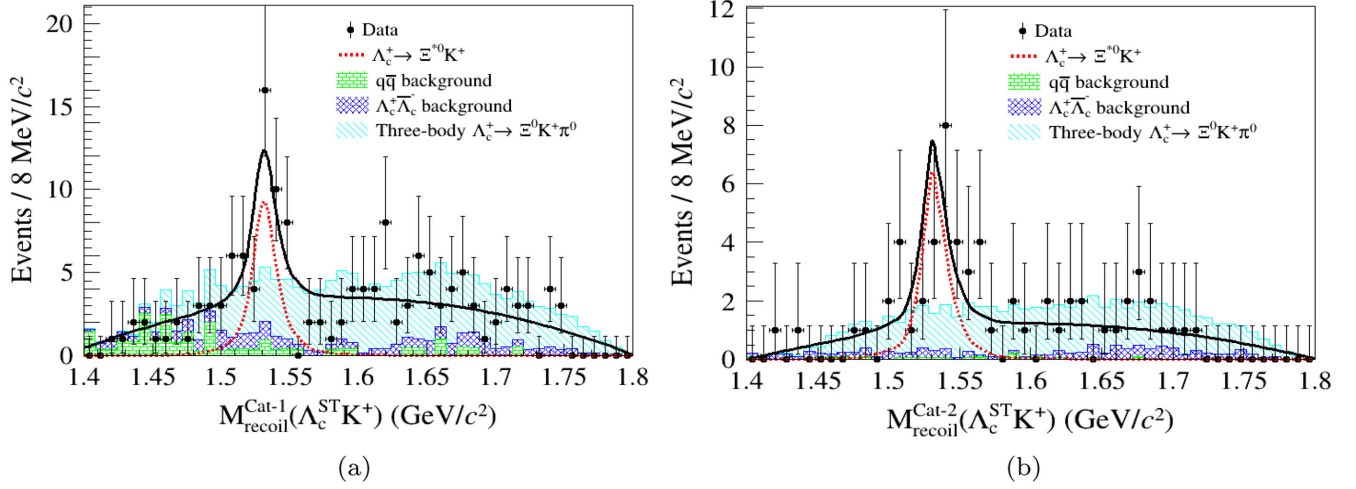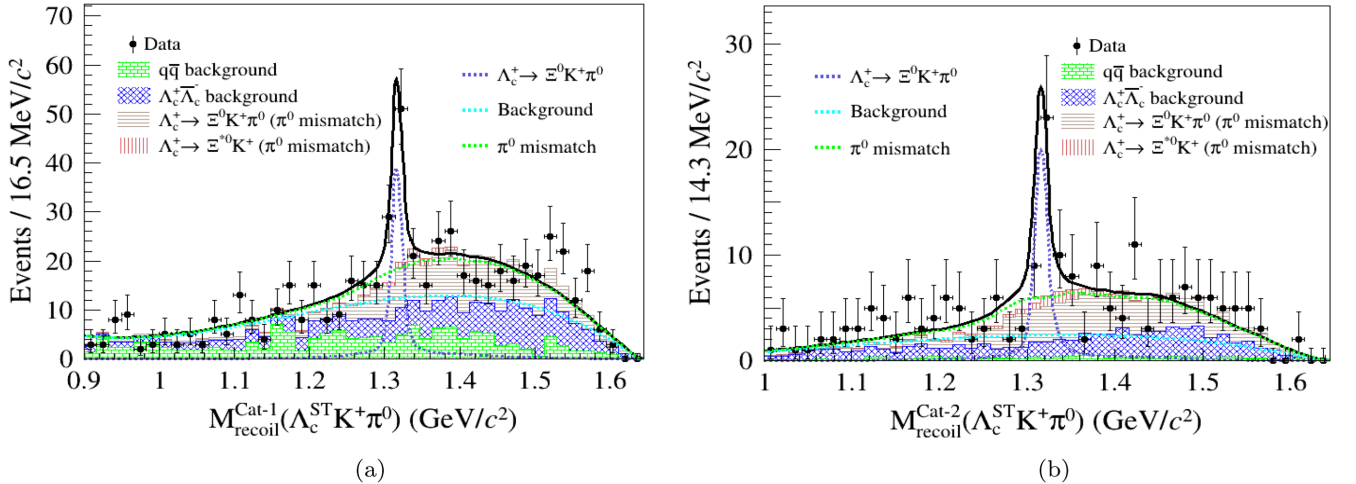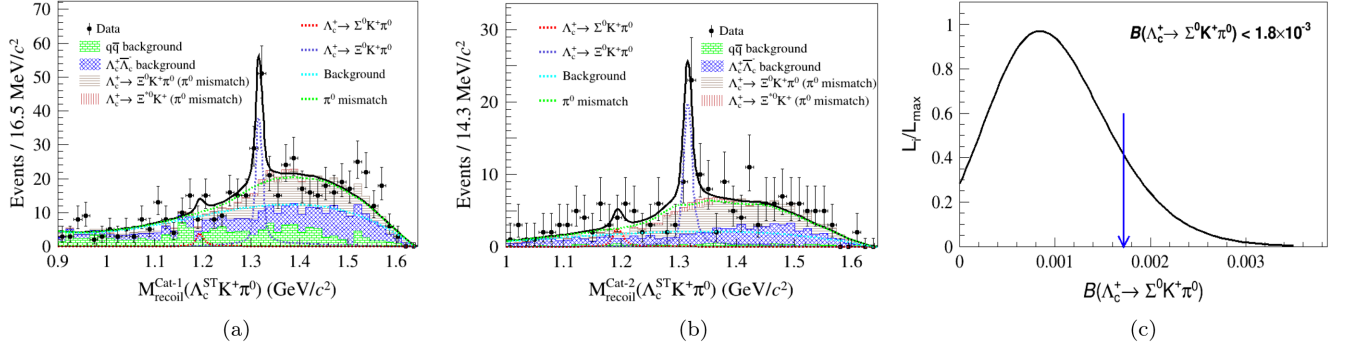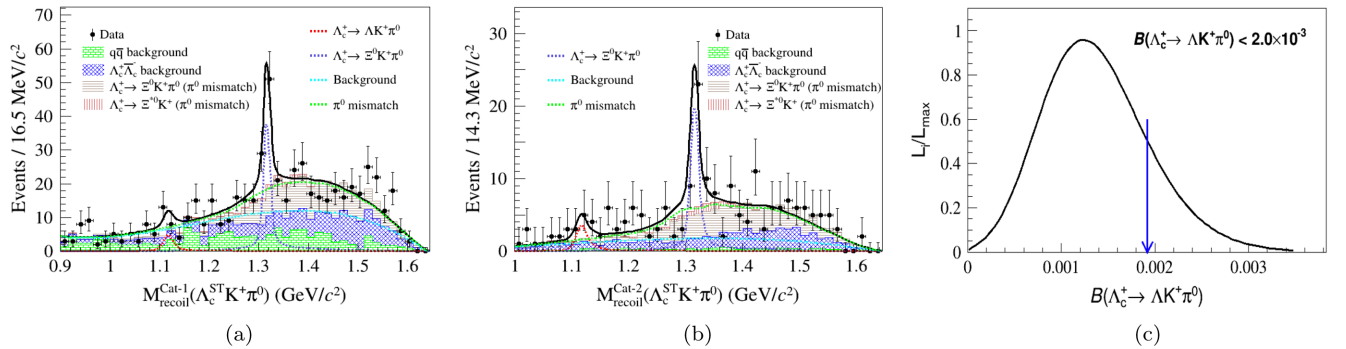
FIG. 4.　The fit projections of (a) $M_{\text{recoil}}^{\text{Cat}-1}(\Lambda_c^{\text{ST}}K^+)$ and (b) $M_{\text{recoil}}^{\text{Cat}-2}(\Lambda_c^{\text{ST}}K^+)$ distributions. The black points with error bars are data. The black line is the sum of all the components in the fit. The blue-shaded histograms are the $\Lambda_c^+\bar{\Lambda}_c^-$ backgrounds. The green-shaded histograms are from the data sideband (in Cat-1) or hadron sample (in Cat-2).

The background shapes are described by third-order polynomial functions, and the background yields are floating. The fitted curves with distributions of $M_{\text{recoil}}^{\text{Cat}-1}(\Lambda_c^{\text{ST}}K^+)$ and $M_{\text{recoil}}^{\text{Cat}-2}(\Lambda_c^{\text{ST}}K^+)$ are shown in Fig. 4. The signal yields are 30 ± 6 and 20 ± 5 events for Cat-1 and Cat-2, respectively. The DT efficiencies in Cat-1 and Cat-2 are summarized in Table III. From Eq. (1), the branching fraction is determined to be $(5.99 \pm 1.04) \times 10^{-3}$, where the uncertainty is statistical. It is consistent with the previous result [48]. The significance, at 6.9σ, is determined by evaluating the difference in likelihood values between fits that include and exclude the signal component, while considering the change in the number of degrees of freedom.

For the three-body decay $\Lambda_c^+ \to \Xi^0 K^+ \pi^0$, the simultaneous fit shares the same branching fraction and takes into account the different detection efficiencies of the individual processes. The fit projections of $M_{\text{recoil}}^{\text{Cat}-1}(\Lambda_c^{\text{ST}}K^+\pi^0)$ and $M_{\text{recoil}}^{\text{Cat}-2}(\Lambda_c^{\text{ST}}K^+\pi^0)$ are shown in Fig. 5, and the total signal yields of $\Lambda_c^+ \to \Xi^0 K^+ \pi^0$ are 57 ± 9 and 40 ± 7 events for Cat-1 and Cat-2, respectively.

The DT efficiencies of Cat-1 and Cat-2 for $\Lambda_c^+ \to \Xi^0 K^+ \pi^0$ are summarized in Table IV. The simulation samples use a flat phase space model, but intermediate resonances could affect the momentum and angular distributions of the final state particles, which would affect

FIG. 5.　Fit projections of (a) $M_{\text{recoil}}^{\text{Cat}-1}(\Lambda_c^{\text{ST}}K^+\pi^0)$ and (b) $M_{\text{recoil}}^{\text{Cat}-2}(\Lambda_c^{\text{ST}}K^+\pi^0)$ distributions. The black points with error bars are data. The black line is the sum of all the components in the fit. The blue-shaded histograms are the $\Lambda_c^+\bar{\Lambda}_c^-$ background. The green-shaded histograms are from the data sideband (in Cat-1) or hadron sample (in Cat-2). The purple line represents the signal shape of the three-body decay $\Lambda_c^+ \to \Xi^0 K^+ \pi^0$. The dashed blue line represents the one-dimensional histogram PDF that describes the background distributions of $M_{\text{recoil}}(\Lambda_c^{\text{ST}}K^+\pi^0)$, which are modeled with an polynomial function.
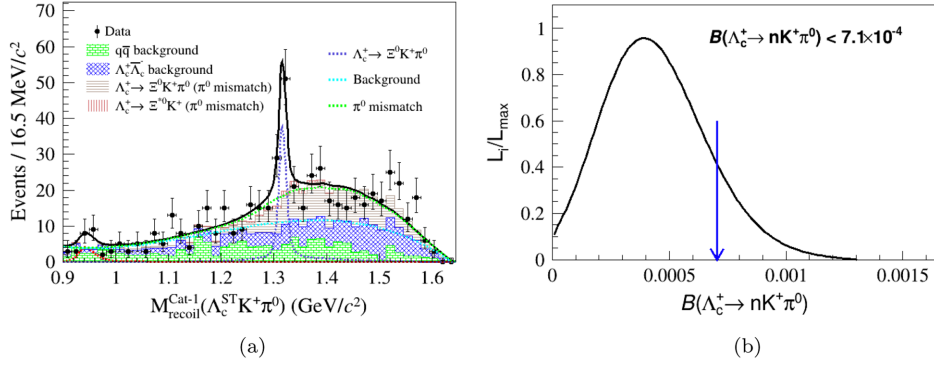
FIG. 6.   Fit projections on (a) $M_{\mathrm{recoil}}^{\mathrm{Cat}-1}(\Lambda_c^{\mathrm{ST}}K^+\pi^0)$ distribution and (b) Likelihood distribution over the branching fractions of $\Lambda_c^+ \to nK^+\pi^0$.

FIG. 7.   Fit projections on (a) $M_{\mathrm{recoil}}^{\mathrm{Cat}-1}(\Lambda_c^{\mathrm{ST}}K^+\pi^0)$, (b) $M_{\mathrm{recoil}}^{\mathrm{Cat}-2}(\Lambda_c^{\mathrm{ST}}K^+\pi^0)$ distributions and (c) Likelihood distributions over the branching fractions of $\Lambda_c^+ \to \Sigma^0 K^+\pi^0$. The black curve denotes the fit result with systematic uncertainty. The blue arrows show the results corresponding to 90% confidence level.

DT efficiencies. Therefore, the simulation samples are reweighted to match data. The two variables, $M(K^+\pi^0)$ and $M_{\mathrm{recoil}}(\Lambda_c^{\mathrm{ST}}\pi^0)$, are selected for the reweighting procedure using a 6×6 binning scheme with uniformly spaced bins. The overall efficiency is 3.44% before the procedure and 3.61% after.

Using the results of fits to $M_{\mathrm{recoil}}^{\mathrm{Cat}-1}(\Lambda_c^{\mathrm{ST}}K^+)$ and $M_{\mathrm{recoil}}^{\mathrm{Cat}-2}(\Lambda_c^{\mathrm{ST}}K^+)$ and correcting for the differences in efficiency, the contributions to the three-body decays

$\Lambda_c^+ \to \Xi^0 K^+\pi^0$ are calculated. After subtracting them, the yields of the three-body decay $\Lambda_c^+ \to \Xi^0 K^+\pi^0$ are 48 ± 9 and 31 ± 7 for Cat-1 and Cat-2, respectively. Using Eq. (1) and the corrected efficiency, the branching fraction is determined to be $(7.79 \pm 1.46) \times 10^{-3}$, where the uncertainty is statistical, and the statistical significance is 8.6σ.

For the three-body decays $\Lambda_c^+ \to nK^+\pi^0$, $\Lambda_c^+ \to \Sigma^0 K^+\pi^0$ and $\Lambda K^+\pi^0$, simultaneous fits are made to the

FIG. 8.   Fit projections on (a) $M_{\mathrm{recoil}}^{\mathrm{Cat}-1}(\Lambda_c^{\mathrm{ST}}K^+\pi^0)$, (b) $M_{\mathrm{recoil}}^{\mathrm{Cat}-2}(\Lambda_c^{\mathrm{ST}}K^+\pi^0)$ distributions and (c) Likelihood distributions over the branching fractions of $\Lambda_c^+ \to \Lambda K^+\pi^0$.

$M_{\text{recoil}}^{\text{Cat}-1}(\Lambda_c^{\text{ST}} K^+ \pi^0)$ and $M_{\text{recoil}}^{\text{Cat}-2}(\Lambda_c^{\text{ST}} K^+ \pi^0)$ distributions as shown in Figs. 6–8. Since no significant signals are observed, the frequentist method is used to determine the upper limits on the branching fractions of these decays [49]. The upper limits, at a 90% confidence level, are determined by integrating the likelihood curves, which are obtained by scanning over the branching fraction.

For the three-body decay $\Lambda_c^+ \to n K^+ \pi^0$, the signal yield is 10 ± 6 events and DT efficiencies in Cat-1 are summarized in Table V. The upper limit on the branching fraction of this decay at the 90% confidence level is $\mathcal{B}(\Lambda_c^+ \to n K^+ \pi^0) < 7.1 \times 10^{-4}$. For the three-body decays $\Lambda_c^+ \to \Sigma^0 K^+ \pi^0$ and $\Lambda K^+ \pi^0$, the signal yields of $\Lambda_c^+ \to \Sigma^0 K^+ \pi^0$ are 7 ± 5 and 6 ± 4 events for Cat-1 and Cat-2, respectively. The signal yields of $\Lambda_c^+ \to \Lambda K^+ \pi^0$ are 10 ± 4 and 10 ± 4 events for Cat-1 and Cat-2, respectively. The DT efficiencies in are summarized in Tables VI and VII, and the upper limits are $\mathcal{B}(\Lambda_c^+ \to \Sigma^0 K^+ \pi^0) < 1.8 \times 10^{-3}$ and $\mathcal{B}(\Lambda_c^+ \to \Lambda K^+ \pi^0) < 2.0 \times 10^{-3}$, respectively. The black solid curves in Figs. 6(b), 7(c) and 8(c) show the resulting likelihood distributions for these three decays.

VII. SYSTEMATIC UNCERTAINTIES

The systematic uncertainties for the branching fraction measurements include those associated with the ST yields (N_i^{ST}), detection efficiencies of the ST $\bar{\Lambda}_c^-$ (ϵ_i^{ST}), detection efficiencies of the DT events (ϵ_i^{DT}) and signal yield (N_{sig}). Since Eq. (1) contains a ratio of ST and DT efficiencies, any systematic uncertainty on the tag side is canceled to first order. Each of them is evaluated relative to the measured branching fraction.

The numbers of charged tracks are required to be only one (Cat-1) or three (Cat-2) without any extra charged tracks. This difference between data and MC simulation for this selection is studied with control sample of $\Lambda_c^+ \to p K^- \pi^+$ (the other $\bar{\Lambda}_c^-$ goes to the 10 tag modes). The uncertainty on the requirement of the number of charged tracks is assigned to be 2.2%, which is denoted as "No extra charged track" in Table VIII.

The tracking efficiencies for K^+ as a function of transverse momentum has been studied with the process $J/\psi \to K_S^0 K^+ \pi^- \to K^+ \pi^+ \pi^- \pi^-$. The efficiency differences between data and MC simulation are both 1% for K^+ tracking and PID efficiencies, which are taken as the systematic uncertainties [50]. The uncertainty associated with the π^0 reconstruction is assigned to be 1.0%, studied with control sample of $J/\psi \to \pi^+ \pi^- \pi^0$ [51].

The uncertainties in the total ST yields are 0.5% [52], which arise from the statistical uncertainty and fitting strategy of extracting ST yields.

The uncertainties of the background and fits of the distributions of $M_{\text{recoil}}^{\text{Cat}-1}(\Lambda_c^{\text{ST}} K^+ \pi^0)$ and $M_{\text{recoil}}^{\text{Cat}-2}(\Lambda_c^{\text{ST}} K^+ \pi^0)$ arise from the sideband range and background estimation. First, the uncertainty for the data sideband and $q\bar{q}$ background estimation is derived from the statistical uncertainty of the background estimate in the M_{BC} sideband region and the variation of the sideband range. Second, the background shape is changed from a polynomial function to an ARGUS function. The differences between the new and nominal results are taken as the systematic uncertainties.

The uncertainty due to the Λ reconstruction efficiency, which is estimated by a weighted root-mean-square of the statistical uncertainties for different (p, $\cos\theta$) intervals, is assigned to be 0.6% using a sample of $J/\psi \to \bar{p} K^+ \Lambda$ decays [53].

The uncertainty due to the π^0 selection combines two sources. The first source is originated from π^0 selection with the minimum kinematic-fit χ^2, which is studied with control sample of $\Lambda_c^+ \to \Sigma^+ \omega$ and $\Lambda_c^+ \to \Sigma^+ \pi^0$. The difference between data and MC simulation is 1%. The second one is due to the π^0 mismatch component, which is evaluated using simulation samples with an alternative π^0 matching approach, where the π^0 candidate closest to the true π^0 is chosen to be the reconstructed π^0 candidate. The fit is performed on the simulation samples, using both the nominal and alternative π^0 matching, and the difference in the fitted branching fraction between them is taken as the systematic uncertainty.

TABLE VIII. Systematic uncertainties (%).

Sources	$\Lambda_c^+ \to \Xi(1530)^0 K^+$		$\Lambda_c^+ \to \Xi^0 K^+ \pi^0$		$\Lambda_c^+ \to \Sigma^0 K^+ \pi^0$		$\Lambda_c^+ \to \Lambda K^+ \pi^0$		$\Lambda_c^+ \to n K^+ \pi^0$
	Cat-1	Cat-2	Cat-1	Cat-2	Cat-1	Cat-2	Cat-1	Cat-2	Cat-1
No extra charged track					2.20				
K^+ tracking					1.00				
K^+ PID					1.00				
π^0 reconstruction					1.00				
ST yield					0.50				
Background PDF	1.17	1.17	3.70	3.70	4.18	4.18	3.68	3.68	3.99
Λ reconstruction		0.60		0.60		0.60		0.60	
π^0 selection	2.23	2.23	5.23	5.23	2.86	2.68	3.56	3.42	4.29
Reweighting			4.95	2.43					
Sum	3.80	3.85	8.58	8.60	5.81	5.76	5.86	5.81	6.51

TABLE IX. The comparison between the measurement and theoretical predictions ($\times 10^{-3}$). The first and the second uncertainties are statistical and systematic, respectively.

	$\Lambda_c^+ \to \Xi(1530)^0 K^+$	$\Lambda_c^+ \to \Xi^0 K^+ \pi^0$	$\Lambda_c^+ \to \Sigma^0 K^+ \pi^0$	$\Lambda_c^+ \to \Lambda K^+ \pi^0$	$\Lambda_c^+ \to n K^+ \pi^0$
This measurement	$5.99 \pm 1.04 \pm 0.32$	$7.79 \pm 1.46 \pm 0.95$	<1.8	<2.0	<0.71
K. K. Sharma *et al.* [23]	$\cdots$	45 ± 8	1.2 ± 0.3	4.5 ± 0.8	0.05 ± 0.005
Jian-Yong Cen *et al.* [24]	$\cdots$	32 ± 6	0.7 ± 0.2	3.5 ± 0.6	0.05 ± 0.006
$\mathcal{B}$(previous results) [48]	$5.02 \pm 0.99 \pm 0.31$	$\cdots$	$\cdots$	$\cdots$	$\cdots$

The uncertainty in reweighting the $\Lambda_c^+ \to \Xi^0 K^+ \pi^0$ simulation samples is derived using different 2D variables and different choices of 2D binning, for instance 6 bins ×6 bins to 7 bins ×7 bins. The uncertainty is determined in a similar manner as the uncertainty from the background shape.

The total systematic uncertainty for the two strategies is obtained by taking the quadratic sum of the individual values. Some systematic uncertainties are the same between two strategies, e.g. tracking and PID of the charged kaon, so they are assumed to be fully correlated in the combination. Other systematic uncertainties are independent between two strategies, e.g. Λ reconstruction, background estimation in the fits on the distributions of $M_{\rm recoil}^{\rm Cat-1}(\Lambda_c^{\rm ST} K^+ \pi^0)$ and $M_{\rm recoil}^{\rm Cat-2}(\Lambda_c^{\rm ST} K^+ \pi^0)$, and they are treated without any correlation in the combination. The different systematic sources are listed in Table VIII, where the two categories have been separated explicitly.

VIII. SUMMARY

With 6.1 fb^{-1} of $e^+ e^-$ collision data collected at eleven CM energy points between 4.600 and 4.840 GeV with the BESIII detector at BEPCII, the CF decays $\Lambda_c^+ \to \Xi^0 K^+ \pi^0$ and $\Lambda_c^+ \to \Xi(1530)^0 K^+$ are observed with significances of 8.6σ and 6.9σ, respectively. The branching fraction of $\Lambda_c^+ \to \Xi^0 K^+ \pi^0$ is measured to be $(7.79 \pm 1.46 \pm 0.95) \times 10^{-3}$, where the first and second uncertainties are statistical and systematic, respectively. It is smaller than the theoretical predictions $(4.5 \pm 0.8) \times 10^{-2}$ [23] and $(3.2 \pm 0.6) \times 10^{-2}$ [24]. Comparisons of theory and experiment are shown in Table IX. The branching fraction of $\Lambda_c^+ \to \Xi(1530)^0 K^+$ is $(5.99 \pm 1.04 \pm 0.32) \times 10^{-3}$, which is consistent with the previous result $(5.02 \pm 0.99 \pm 0.31) \times 10^{-3}$ [48].

The upper limits on the branching fractions at the 90% confidence level of the SCS or DCS decays $\Lambda_c^+ \to n K^+ \pi^0$, $\Sigma^0 K^+ \pi^0$ and $\Lambda K^+ \pi^0$ are 7.1×10^{-4}, 1.8×10^{-3} and 2.0×10^{-3}, respectively. The upper limit of the branching fraction of $\Lambda_c^+ \to \Lambda K^+ \pi^0$ is incompatible with the theory predictions [23,24]. The upper limits of the branching fractions of $\Lambda_c^+ \to \Sigma^0 K^+ \pi^0$ and $\Lambda_c^+ \to n K^+ \pi^0$ are consistent with the theoretical predictions [23,24]. These results are essential for the understanding of the dynamics in the charmed baryon decays.

[1] H. Y. Cheng, Front. Phys. **10**, 101406 (2015).

[2] C. D. Lü, W. Wang, and F. S. Yu, Phys. Rev. D **93**, 056008 (2016).

[3] M. A. Ivanov, J. G. Korner, V. E. Lyubovitskij, and A. G. Rusetsky, Phys. Rev. D **57**, 5632 (1998).

[4] K. K. Sharma and R. C. Verma, Phys. Rev. D **55**, 7067 (1997).

[5] T. Uppal, R. C. Verma, and M. P. Khanna, Phys. Rev. D **49**, 3417 (1994).

[6] P. Zenczykowski, Phys. Rev. D **50**, 402 (1994).

[7] J. G. Korner and M. Kramer, Z. Phys. C **55**, 659 (1992).

[8] J. G. Korner, G. Kramer, and J. Willrodt, Z. Phys. C **2**, 117 (1979).

[9] M. Ablikim *et al.* (BESIII Collaboration), Phys. Rev. Lett. **117**, 232002 (2016).

[10] C. Q. Geng, C. W. Liu, and T. H. Tsai, Phys. Lett. B **790**, 225 (2019).

[11] H. Y. Cheng, X. W. Kang, and F. Xu, Phys. Rev. D **97**, 074028 (2018).

[12] Geng C. and Zhou X., Symmetry **15**, 20 (2023).

[13] G. Meng, S. M. Y. Wong, and F. R. Xu, J. High Energy Phys. 11 (2020) 126.

[14] B. L. Wang, Nucl. Part. Phys. Proc. **294**, 95 (2018).

[15] S. X. Li *et al.* (Belle Collaboration), Phys. Rev. D **103**, 072004 (2021).

[16] R. Aaij *et al.* (LHCb Collaboration), J. High Energy Phys. 03 (2018) 182.

[17] M. Ablikim *et al.* (BESIII Collaboration), Phys. Rev. Lett. **128**, 142001 (2022).

[18] M. Ablikim *et al.* (BESIII Collaboration), Phys. Rev. Lett. **120**, 132001 (2018).

[19] M. Ablikim *et al.* (BESIII Collaboration), Phys. Rev. D **95**, 111102 (2017).

[20] M. Ablikim *et al.* (BESIII Collaboration), Phys. Rev. Lett. **129**, 231803 (2022).

[21] M. Ablikim *et al.* (BESIII Collaboration), Phys. Rev. Lett. **116**, 052001 (2016).

[22] A. Zupanc *et al.* (Belle Collaboration), Phys. Rev. Lett. **113**, 042002 (2014).

[23] C. Q. Geng, Y. K. Hsiao, C. W. Liu, and T. H. Tsai, Phys. Rev. D **99**, 073003 (2019).

[24] J. Y. Cen, C. Q. Geng, C. W. Liu, and T. H. Tsai, Eur. Phys. J. C **79**, 946 (2019).

[25] S. B. Yang *et al.* (Belle Collaboration), Phys. Rev. Lett. **117**, 011801 (2016).

[26] J. Adler *et al.* (Mark III Collaboration), Phys. Rev. Lett. **62**, 1821 (1989).

[27] M. Ablikim *et al.* (BESIII Collaboration), Chin. Phys. C **40**, 063001 (2016).

[28] M. Ablikim *et al.* (BESIII Collaboration), Chin. Phys. C **46**, 113003 (2022).

[29] M. Ablikim *et al.* (BESIII Collaboration), Nucl. Instrum. Methods Phys. Res., Sect. A **614**, 345 (2010).

[30] C. H. Yu *et al.*, *Proceedings of IPAC2016, Busan, Korea* (JACoW, Geneva, Switzerland, 2016).

[31] M. Ablikim *et al.* (BESIII Collaboration), Chin. Phys. C **44**, 040001 (2020).

[32] K. X. Huang *et al.*, Nucl. Sci. Tech. **33**, 142 (2022).

[33] X. Li *et al.*, Radiat. Detect. Technol. Methods **1**, 13 (2017).

[34] S. Agostinelli *et al.* (GEANT4 Collaboration), Nucl. Instrum. Methods Phys. Res., Sect. A **506**, 250 (2003).

[35] Y. Liang *et al.*, Nucl. Instrum. Methods Phys. Res., Sect. A **603**, 325 (2009).

[36] Z. Y. You, Y. T. Liang, and Y. J. Mao, Chin. Phys. C **32**, 572 (2008).

[37] R. L. Workman *et al.* (Particle Data Group), Prog. Theor. Exp. Phys. **2022**, 083C01 (2022).

[38] M. Ablikim *et al.* (BESIII Collaboration), Phys. Rev. D **106**, 072002 (2022).

[39] S. Jadach, B. F. L. Ward, and Z. Was, Phys. Rev. D **63**, 113009 (2001).

[40] S. Jadach, B. F. L. Ward, and Z. Was, Comput. Phys. Commun. **130**, 260 (2000).

[41] D. J. Lange, Nucl. Instrum. Methods Phys. Res., Sect. A **462**, 152 (2001).

[42] R. G. Ping, Chin. Phys. C **32**, 599 (2008).

[43] J. C. Chen, G. S. Huang, X. R. Qi, D. H. Zhang, and Y. S. Zhu, Phys. Rev. D **62**, 034003 (2000).

[44] R. L. Yang, R. G. Ping, and H. Chen, Chin. Phys. Lett. **31**, 061301 (2014).

[45] E. Richter-Was, Phys. Lett. B **303**, 163 (1993).

[46] H. Albrecht *et al.* (ARGUS Collaboration), Phys. Lett. B **241**, 278 (1990).

[47] M. Xu *et al.*, Chin. Phys. C **33**, 428 (2009).

[48] M. Ablikim *et al.* (BESIII Collaboration), Phys. Lett. B **783**, 200 (2018).

[49] W. A. Rolke, A. M. Lopez, and J. Conrad, Nucl. Instrum. Methods Phys. Res., Sect. A **551**, 493 (2005).

[50] M. Ablikim *et al.* (BESIII Collaboration), Phys. Rev. D **99**, 012003 (2019).

[51] M. Ablikim *et al.* (BESIII Collaboration), Phys. Rev. D **96**, 112012 (2017).

[52] M. Ablikim *et al.* (BESIII Collaboration), Phys. Rev. D **106**, 072008 (2022).

[53] M. Ablikim *et al.* (BESIII Collaboration), Phys. Rev. Lett. **121**, 062003 (2018).

M. Ablikim,[1] M. N. Achasov,[5,c] P. Adlarson,[75] O. Afedulidis,[4] X. C. Ai,[80] R. Aliberti,[36] A. Amoroso,[74a,74c] M. R. An,[40] Q. An,[71,58,a] Y. Bai,[57] O. Bakina,[37] I. Balossino,[30a] Y. Ban,[47,h] V. Batozskaya,[1,45] K. Begzsuren,[33] N. Berger,[36] M. Berlowski,[45] M. Bertani,[29a] D. Bettoni,[30a] F. Bianchi,[74a,74c] E. Bianco,[74a,74c] A. Bortone,[74a,74c] I. Boyko,[37] R. A. Briere,[6] A. Brueggemann,[68] H. Cai,[76] X. Cai,[1,58] A. Calcaterra,[29a] G. F. Cao,[1,63] N. Cao,[1,63] S. A. Cetin,[62a] J. F. Chang,[1,58] G. R. Che,[44] G. Chelkov,[37,b] C. Chen,[44] Chao Chen,[55] G. Chen,[1] H. S. Chen,[1,63] M. L. Chen,[1,58,63] S. J. Chen,[43] S. L. Chen,[46] S. M. Chen,[61] T. Chen,[1,63] X. R. Chen,[32,63] X. T. Chen,[1,63] Y. B. Chen,[1,58] Y. Q. Chen,[35] Z. J. Chen,[26,i] Z. Y. Chen,[1,63] S. K. Choi,[11a] X. Chu,[44] G. Cibinetto,[30a] S. C. Coen,[4] F. Cossio,[74c] J. J. Cui,[50] H. L. Dai,[1,58] J. P. Dai,[78] A. Dbeyssi,[19]

R. E. de Boer,[4] D. Dedovich,[37] Z. Y. Deng,[1] A. Denig,[36] I. Denysenko,[37] M. Destefanis,[74a,74c] F. De Mori,[74a,74c] B. Ding,[66,1] X. X. Ding,[47,h] Y. Ding,[35] Y. Ding,[41] J. Dong,[1,58] L. Y. Dong,[1,63] M. Y. Dong,[1,58,63] X. Dong,[76] M. C. Du,[1] S. X. Du,[80] Z. H. Duan,[43] P. Egorov,[37,b] Y. H. Fan,[46] Y. L. Fan,[76] J. Fang,[1,58] S. S. Fang,[1,63] W. X. Fang,[1] Y. Fang,[1] R. Farinelli,[30a] L. Fava,[74b,74c] F. Feldbauer,[4] G. Felici,[29a] C. Q. Feng,[71,58] J. H. Feng,[59] K. Fischer,[69] M. Fritsch,[4] C. D. Fu,[1] J. L. Fu,[63] Y. W. Fu,[1,63] H. Gao,[63] Y. N. Gao,[47,h] Yang Gao,[71,58] S. Garbolino,[74c] I. Garzia,[30a,30b] L. Ge,[80] P. T. Ge,[76] Z. W. Ge,[43] C. Geng,[59] E. M. Gersabeck,[67] A. Gilman,[69] K. Goetzen,[14] L. Gong,[41] W. X. Gong,[1,58] W. Gradl,[36] S. Gramigna,[30a,30b] M. Greco,[74a,74c] M. H. Gu,[1,58] Y. T. Gu,[16] C. Y. Guan,[1,63] Z. L. Guan,[23] A. Q. Guo,[32,63] L. B. Guo,[42] M. J. Guo,[50] R. P. Guo,[49] Y. P. Guo,[13,g] A. Guskov,[37,b] T. T. Han,[50] W. Y. Han,[40] X. Q. Hao,[20] F. A. Harris,[65] K. K. He,[55] K. L. He,[1,63] F. H. Heinsius,[4] C. H. Heinz,[36] Y. K. Heng,[1,58,63] C. Herold,[60] T. Holtmann,[4] P. C. Hong,[13,g] G. Y. Hou,[1,63] X. T. Hou,[1,63] Y. R. Hou,[63] Z. L. Hou,[1] B. Y. Hu,[59] H. M. Hu,[1,63] J. F. Hu,[56,j] T. Hu,[1,58,63] Y. Hu,[1] G. S. Huang,[71,58] K. X. Huang,[59] L. Q. Huang,[32,63] X. T. Huang,[50] Y. P. Huang,[1] T. Hussain,[73] F. Hölzken,[4] N. Hüsken,[28,36] W. Imoehl,[28] J. Jackson,[28] S. Jaeger,[4] S. Janchiv,[33] J. H. Jeong,[11a] Q. Ji,[1] Q. P. Ji,[20] X. B. Ji,[1,63] X. L. Ji,[1,58] Y. Y. Ji,[50] X. Q. Jia,[50] Z. K. Jia,[71,58] H. B. Jiang,[76] P. C. Jiang,[47,h] S. S. Jiang,[40] T. J. Jiang,[17] X. S. Jiang,[1,58,63] Y. Jiang,[63] J. B. Jiao,[50] Z. Jiao,[24] S. Jin,[43] Y. Jin,[66] M. Q. Jing,[1,63] T. Johansson,[75] S. Kabana,[34] N. Kalantar-Nayestanaki,[64] X. L. Kang,[10] X. S. Kang,[41] R. Kappert,[64] M. Kavatsyuk,[64] B. C. Ke,[80] A. Khoukaz,[68] R. Kiuchi,[1] R. Kliemt,[14] O. B. Kolcu,[62a] B. Kopf,[4] M. Kuessner,[4] X. Kui,[1,63] N. Kumar,[27] A. Kupsc,[45,75] W. Kühn,[38] J. J. Lane,[67] P. Larin,[19] A. Lavania,[27] L. Lavezzi,[74a,74c] T. T. Lei,[71,58] Z. H. Lei,[71,58] M. Lellmann,[36] T. Lenz,[36] C. Li,[48] C. Li,[44] C. H. Li,[40] Cheng Li,[71,58] D. M. Li,[80] F. Li,[1,58] G. Li,[1] H. B. Li,[1,63] H. J. Li,[20] H. N. Li,[56,j] Hui Li,[44] J. R. Li,[61] J. S. Li,[59] J. W. Li,[50] K. Li,[1] K. L. Li,[20] L. J. Li,[1,63] L. K. Li,[1] Lei Li,[3] M. H. Li,[44] P. R. Li,[39,k,l] Q. X. Li,[50] S. X. Li,[13] T. Li,[50] W. D. Li,[1,63] W. G. Li,[1,a] X. H. Li,[71,58] X. L. Li,[50] X. Y. Li,[1,63] Y. G. Li,[47,h] Z. J. Li,[59] Z. X. Li,[16] C. Liang,[43] H. Liang,[1,63] H. Liang,[71,58] H. Liang,[35] Y. F. Liang,[54] Y. T. Liang,[32,63] G. R. Liao,[15] L. Z. Liao,[50] Y. P. Liao,[1,63] J. Libby,[27] A. Limphirat,[60] D. X. Lin,[32,63] T. Lin,[1] B. J. Liu,[1] B. X. Liu,[76] C. Liu,[35] C. X. Liu,[1] F. Liu,[1] F. H. Liu,[53] Feng Liu,[7] G. M. Liu,[56,j] H. Liu,[39,k,l] H. B. Liu,[16] H. H. Liu,[1] H. M. Liu,[1,63] Huihui Liu,[22] J. B. Liu,[71,58] J. L. Liu,[72] J. Y. Liu,[1,63] K. Liu,[1] K. Y. Liu,[41] Ke Liu,[23] L. Liu,[71,58] L. C. Liu,[44] Lu Liu,[44] M. H. Liu,[13,g] P. L. Liu,[1] Q. Liu,[63] S. B. Liu,[71,58] T. Liu,[13,g] W. K. Liu,[44] W. M. Liu,[71,58] X. Liu,[39,k,l] Y. Liu,[80] Y. Liu,[39,k,l] Y. B. Liu,[44] Z. A. Liu,[1,58,63] Z. Q. Liu,[50] X. C. Lou,[1,58,63] F. X. Lu,[59] H. J. Lu,[24] J. G. Lu,[1,58] X. L. Lu,[1] Y. Lu,[8] Y. P. Lu,[1,58] Z. H. Lu,[1,63] C. L. Luo,[42] M. X. Luo,[79] T. Luo,[13,g] X. L. Luo,[1,58] X. R. Lyu,[63] Y. F. Lyu,[44] F. C. Ma,[41] H. L. Ma,[1] J. L. Ma,[1,63] L. L. Ma,[50] M. M. Ma,[1,63] Q. M. Ma,[1] R. Q. Ma,[1,63] R. T. Ma,[63] X. Y. Ma,[1,58] Y. Ma,[47,h] Y. M. Ma,[32] F. E. Maas,[19] M. Maggiora,[74a,74c] S. Malde,[69] A. Mangoni,[29b] Y. J. Mao,[47,h] Z. P. Mao,[1] S. Marcello,[74a,74c] Z. X. Meng,[66] J. G. Messchendorp,[14,64] G. Mezzadri,[30a] H. Miao,[1,63] T. J. Min,[43] R. E. Mitchell,[28] X. H. Mo,[1,58,63] N. Yu. Muchnoi,[5,c] J. Muskalla,[36] Y. Nefedov,[37] F. Nerling,[19,e] I. B. Nikolaev,[5,c] Z. Ning,[1,58] S. Nisar,[12,m] Y. Niu,[50] S. L. Olsen,[63] Q. Ouyang,[1,58,63] S. Pacetti,[29b,29c] X. Pan,[55] Y. Pan,[57] A. Pathak,[35] P. Patteri,[29a] Y. P. Pei,[71,58] M. Pelizaeus,[4] H. P. Peng,[71,58] K. Peters,[14,e] J. L. Ping,[42] R. G. Ping,[1,63] S. Plura,[36] S. Pogodin,[37] V. Prasad,[34] F. Z. Qi,[1] H. Qi,[71,58] H. R. Qi,[61] M. Qi,[43] T. Y. Qi,[13,g] S. Qian,[1,58] W. B. Qian,[63] C. F. Qiao,[63] X. K. Qiao,[80] J. J. Qin,[72] L. Q. Qin,[15] X. P. Qin,[13,g] X. S. Qin,[50] Z. H. Qin,[1,58] J. F. Qiu,[1] S. Q. Qu,[61] C. F. Redmer,[36] K. J. Ren,[40] A. Rivetti,[74c] V. Rodin,[64] M. Rolo,[74c] G. Rong,[1,63] Ch. Rosner,[19] S. N. Ruan,[44] N. Salone,[45] A. Sarantsev,[37,d] Y. Schelhaas,[36] K. Schoenning,[75] M. Scodeggio,[30a] K. Y. Shan,[13,g] W. Shan,[25] X. Y. Shan,[71,58] J. F. Shangguan,[55] L. G. Shao,[1,63] M. Shao,[71,58] C. P. Shen,[13,g] H. F. Shen,[1,9] W. H. Shen,[63] X. Y. Shen,[1,63] B. A. Shi,[63] H. C. Shi,[71,58] J. L. Shi,[13,g] J. Y. Shi,[1] Q. Q. Shi,[55] X. Shi,[1,58] J. J. Song,[20] T. Z. Song,[59] W. M. Song,[35,1] Y. J. Song,[13,g] Y. X. Song,[47,h,n] S. Sosio,[74a,74c] S. Spataro,[74a,74c] F. Stieler,[36] Y. J. Su,[63] G. B. Sun,[76] G. X. Sun,[1] H. Sun,[63] H. K. Sun,[1] J. F. Sun,[20] K. Sun,[61] L. Sun,[76] S. S. Sun,[1,63] T. Sun,[1,63] T. Sun,[51,f] W. Y. Sun,[35] Y. Sun,[10] Y. J. Sun,[71,58] Y. Z. Sun,[1] Z. T. Sun,[50] C. J. Tang,[54] G. Y. Tang,[1] J. Tang,[59] Y. A. Tang,[76] L. Y. Tao,[72] Q. T. Tao,[26,i] M. Tat,[69] J. X. Teng,[71,58] V. Thoren,[75] W. H. Tian,[52] W. H. Tian,[59] Y. Tian,[32,63] Z. F. Tian,[76] I. Uman,[62b] S. J. Wang,[50] B. Wang,[1] B. L. Wang,[63] Bo Wang,[71,58] C. W. Wang,[43] D. Y. Wang,[47,h] F. Wang,[72] H. J. Wang,[39,k,l] H. P. Wang,[1,63] J. P. Wang,[50] K. Wang,[1,58] L. L. Wang,[1] M. Wang,[50] S. Wang,[39,k,l] S. Wang,[13,g] T. Wang,[13,g] T. J. Wang,[44] W. Wang,[72] W. Wang,[59] W. P. Wang,[71,58] W. P. Wang,[36,71,o] X. Wang,[47,h] X. F. Wang,[39,k,l] X. J. Wang,[40] X. L. Wang,[13,g] Y. Wang,[61] Y. D. Wang,[46] Y. F. Wang,[1,58,63] Y. H. Wang,[48] Y. N. Wang,[46] Y. Q. Wang,[1] Yaqian Wang,[18] Yi Wang,[61] Z. Wang,[1,58] Z. L. Wang,[72] Z. Y. Wang,[1,63] Ziyi Wang,[63] D. H. Wei,[15] F. Weidner,[68] S. P. Wen,[1] C. Wenzel,[4] U. Wiedner,[4] G. Wilkinson,[69] M. Wolke,[75] L. Wollenberg,[4] C. Wu,[40] J. F. Wu,[1,9] L. H. Wu,[1] L. J. Wu,[1,63] X. Wu,[13,g] X. H. Wu,[35] Y. Wu,[71,58] Y. J. Wu,[32] Z. Wu,[1,58] L. Xia,[71,58] X. M. Xian,[40] T. Xiang,[47,h] D. Xiao,[39,k,l] G. Y. Xiao,[43] S. Y. Xiao,[1] Y. L. Xiao,[13,g] Z. J. Xiao,[42] C. Xie,[43] X. H. Xie,[47,h] Y. Xie,[50] Y. G. Xie,[1,58] Y. H. Xie,[7] Z. P. Xie,[71,58] T. Y. Xing,[1,63] C. F. Xu,[1,63] C. J. Xu,[59] G. F. Xu,[1] H. Y. Xu,[66,2,p] M. Xu,[71,58] Q. J. Xu,[17] Q. N. Xu,[31] W. Xu,[1] W. L. Xu,[66] X. P. Xu,[55] Y. C. Xu,[77] Z. P. Xu,[43] Z. S. Xu,[63] F. Yan,[13,g] L. Yan,[13,g]

W. B. Yan,[71,58] W. C. Yan,[80] X. Q. Yan,[1,63] H. J. Yang,[51,f] H. L. Yang,[35] H. X. Yang,[1] T. Yang,[1] Y. Yang,[13,g] Y. F. Yang,[1,63] Y. F. Yang,[44] Y. X. Yang,[1,63] Z. W. Yang,[39,k,l] Z. P. Yao,[50] M. Ye,[1,58] M. H. Ye,[9] J. H. Yin,[1] Z. Y. You,[59] B. X. Yu,[1,58,63] C. X. Yu,[44] G. Yu,[1,63] J. S. Yu,[26,i] T. Yu,[72] X. D. Yu,[47,h] Y. C. Yu,[80] C. Z. Yuan,[1,63] L. Yuan,[2] S. C. Yuan,[1,63] X. Q. Yuan,[1] Y. Yuan,[1,63] Z. Y. Yuan,[59] C. X. Yue,[40] A. A. Zafar,[73] F. R. Zeng,[50] X. Zeng,[13,g] Y. Zeng,[26,i] X. Y. Zhai,[35] Y. C. Zhai,[50] Y. H. Zhan,[59] A. Q. Zhang,[1,63] B. L. Zhang,[1,63] B. X. Zhang,[1] D. H. Zhang,[44] G. Y. Zhang,[20] H. Zhang,[71,58] H. H. Zhang,[35] H. H. Zhang,[59] H. Q. Zhang,[1,58,63] H. Y. Zhang,[1,58] J. Zhang,[80] J. J. Zhang,[52] J. L. Zhang,[21] J. Q. Zhang,[42] J. W. Zhang,[1,58,63] J. W. Zhang,[1,63] J. X. Zhang,[39,k,l] J. Y. Zhang,[1] J. Z. Zhang,[1,63] Jianyu Zhang,[63] L. M. Zhang,[61] Lei Zhang,[43] P. Zhang,[1,63] Q. Y. Zhang,[40,80] S. H. Zhang,[1,63] Shulei Zhang,[26,i] X. D. Zhang,[46] X. M. Zhang,[1] X. Y. Zhang,[50] Xuyan Zhang,[55] Y. Zhang,[1] Y. Zhang,[72] Y. T. Zhang,[80] Y. H. Zhang,[1,58] Yan Zhang,[71,58] Z. H. Zhang,[1] Z. L. Zhang,[35] Z. Y. Zhang,[76] Z. Y. Zhang,[44] G. Zhao,[1] J. Zhao,[40] J. Y. Zhao,[1,63] J. Z. Zhao,[1,58] L. Zhao,[1] Lei Zhao,[71,58] M. G. Zhao,[44] S. J. Zhao,[80] Y. B. Zhao,[1,58] Y. X. Zhao,[32,63] Z. G. Zhao,[71,58] A. Zhemchugov,[37,b] B. Zheng,[72] J. P. Zheng,[1,58] W. J. Zheng,[1,63] Y. H. Zheng,[63] B. Zhong,[42] X. Zhong,[59] H. Zhou,[50] L. P. Zhou,[1,63] S. Zhou,[7] X. Zhou,[76] X. K. Zhou,[7] X. R. Zhou,[71,58] X. Y. Zhou,[40] Y. Z. Zhou,[13,g] J. Zhu,[44] K. Zhu,[1] K. J. Zhu,[1,58,63] L. Zhu,[35] L. X. Zhu,[63] S. H. Zhu,[70] S. Q. Zhu,[43] T. J. Zhu,[13,g] W. J. Zhu,[13,g] Y. C. Zhu,[71,58] Z. A. Zhu,[1,63] J. H. Zou,[1] and J. Zu[71,58]

(BESIII Collaboration)

[1]*Institute of High Energy Physics, Beijing 100049, People's Republic of China*
[2]*Beihang University, Beijing 100191, People's Republic of China*
[3]*Beijing Institute of Petrochemical Technology, Beijing 102617, People's Republic of China*
[4]*Bochum Ruhr-University, D-44780 Bochum, Germany*
[5]*Budker Institute of Nuclear Physics SB RAS (BINP), Novosibirsk 630090, Russia*
[6]*Carnegie Mellon University, Pittsburgh, Pennsylvania 15213, USA*
[7]*Central China Normal University, Wuhan 430079, People's Republic of China*
[8]*Central South University, Changsha 410083, People's Republic of China*
[9]*China Center of Advanced Science and Technology, Beijing 100190, People's Republic of China*
[10]*China University of Geosciences, Wuhan 430074, People's Republic of China*
[11]*Chung-Ang University, Seoul, 06974, Republic of Korea*
[12]*COMSATS University Islamabad, Lahore Campus, Defence Road, Off Raiwind Road, 54000 Lahore, Pakistan*
[13]*Fudan University, Shanghai 200433, People's Republic of China*
[14]*GSI Helmholtzcentre for Heavy Ion Research GmbH, D-64291 Darmstadt, Germany*
[15]*Guangxi Normal University, Guilin 541004, People's Republic of China*
[16]*Guangxi University, Nanning 530004, People's Republic of China*
[17]*Hangzhou Normal University, Hangzhou 310036, People's Republic of China*
[18]*Hebei University, Baoding 071002, People's Republic of China*
[19]*Helmholtz Institute Mainz, Staudinger Weg 18, D-55099 Mainz, Germany*
[20]*Henan Normal University, Xinxiang 453007, People's Republic of China*
[21]*Henan University, Kaifeng 475004, People's Republic of China*
[22]*Henan University of Science and Technology, Luoyang 471003, People's Republic of China*
[23]*Henan University of Technology, Zhengzhou 450001, People's Republic of China*
[24]*Huangshan College, Huangshan 245000, People's Republic of China*
[25]*Hunan Normal University, Changsha 410081, People's Republic of China*
[26]*Hunan University, Changsha 410082, People's Republic of China*
[27]*Indian Institute of Technology Madras, Chennai 600036, India*
[28]*Indiana University, Bloomington, Indiana 47405, USA*
[29a]*INFN Laboratori Nazionali di Frascati, I-00044, Frascati, Italy*
[29b]*INFN Sezione di Perugia, I-06100, Perugia, Italy*
[29c]*University of Perugia, I-06100, Perugia, Italy*
[30a]*INFN Sezione di Ferrara, I-44122, Ferrara, Italy*
[30b]*University of Ferrara, I-44122, Ferrara, Italy*
[31]*Inner Mongolia University, Hohhot 010021, People's Republic of China*
[32]*Institute of Modern Physics, Lanzhou 730000, People's Republic of China*
[33]*Institute of Physics and Technology, Peace Avenue 54B, Ulaanbaatar 13330, Mongolia*
[34]*Instituto de Alta Investigación, Universidad de Tarapacá, Casilla 7D, Arica 1000000, Chile*
[35]*Jilin University, Changchun 130012, People's Republic of China*

[36]*Johannes Gutenberg University of Mainz, Johann-Joachim-Becher-Weg 45, D-55099 Mainz, Germany*
[37]*Joint Institute for Nuclear Research, 141980 Dubna, Moscow region, Russia*
[38]*Justus-Liebig-Universitaet Giessen, II. Physikalisches Institut,*
Heinrich-Buff-Ring 16, D-35392 Giessen, Germany
[39]*Lanzhou University, Lanzhou 730000, People's Republic of China*
[40]*Liaoning Normal University, Dalian 116029, People's Republic of China*
[41]*Liaoning University, Shenyang 110036, People's Republic of China*
[42]*Nanjing Normal University, Nanjing 210023, People's Republic of China*
[43]*Nanjing University, Nanjing 210093, People's Republic of China*
[44]*Nankai University, Tianjin 300071, People's Republic of China*
[45]*National Centre for Nuclear Research, Warsaw 02-093, Poland*
[46]*North China Electric Power University, Beijing 102206, People's Republic of China*
[47]*Peking University, Beijing 100871, People's Republic of China*
[48]*Qufu Normal University, Qufu 273165, People's Republic of China*
[49]*Shandong Normal University, Jinan 250014, People's Republic of China*
[50]*Shandong University, Jinan 250100, People's Republic of China*
[51]*Shanghai Jiao Tong University, Shanghai 200240, People's Republic of China*
[52]*Shanxi Normal University, Linfen 041004, People's Republic of China*
[53]*Shanxi University, Taiyuan 030006, People's Republic of China*
[54]*Sichuan University, Chengdu 610064, People's Republic of China*
[55]*Soochow University, Suzhou 215006, People's Republic of China*
[56]*South China Normal University, Guangzhou 510006, People's Republic of China*
[57]*Southeast University, Nanjing 211100, People's Republic of China*
[58]*State Key Laboratory of Particle Detection and Electronics, Beijing 100049,*
Hefei 230026, People's Republic of China
[59]*Sun Yat-Sen University, Guangzhou 510275, People's Republic of China*
[60]*Suranaree University of Technology, University Avenue 111, Nakhon Ratchasima 30000, Thailand*
[61]*Tsinghua University, Beijing 100084, People's Republic of China*
[62a]*Turkish Accelerator Center Particle Factory Group, Istinye University, 34010, Istanbul, Turkey*
[62b]*Near East University, Nicosia, North Cyprus, 99138, Mersin 10, Turkey*
[63]*University of Chinese Academy of Sciences, Beijing 100049, People's Republic of China*
[64]*University of Groningen, NL-9747 AA Groningen, The Netherlands*
[65]*University of Hawaii, Honolulu, Hawaii 96822, USA*
[66]*University of Jinan, Jinan 250022, People's Republic of China*
[67]*University of Manchester, Oxford Road, Manchester, M13 9PL, United Kingdom*
[68]*University of Muenster, Wilhelm-Klemm-Strasse 9, 48149 Muenster, Germany*
[69]*University of Oxford, Keble Road, Oxford OX13RH, United Kingdom*
[70]*University of Science and Technology Liaoning, Anshan 114051, People's Republic of China*
[71]*University of Science and Technology of China, Hefei 230026, People's Republic of China*
[72]*University of South China, Hengyang 421001, People's Republic of China*
[73]*University of the Punjab, Lahore-54590, Pakistan*
[74a]*University of Turin and INFN, University of Turin, I-10125, Turin, Italy*
[74b]*University of Eastern Piedmont, I-15121, Alessandria, Italy*
[74c]*INFN, I-10125, Turin, Italy*
[75]*Uppsala University, Box 516, SE-75120 Uppsala, Sweden*
[76]*Wuhan University, Wuhan 430072, People's Republic of China*
[77]*Yantai University, Yantai 264005, People's Republic of China*
[78]*Yunnan University, Kunming 650500, People's Republic of China*
[79]*Zhejiang University, Hangzhou 310027, People's Republic of China*
[80]*Zhengzhou University, Zhengzhou 450001, People's Republic of China*

[a]Deceased.

[b]Also at the Moscow Institute of Physics and Technology, Moscow 141700, Russia.

[c]Also at the Novosibirsk State University, Novosibirsk, 630090, Russia.

[d]Also at the NRC "Kurchatov Institute", PNPI, 188300, Gatchina, Russia.

[e]Also at Goethe University Frankfurt, 60323 Frankfurt am Main, Germany.

[f]Also at Key Laboratory for Particle Physics, Astrophysics and Cosmology, Ministry of Education; Shanghai Key Laboratory for Particle Physics and Cosmology; Institute of Nuclear and Particle Physics, Shanghai 200240, People's Republic of China.

[g]Also at Key Laboratory of Nuclear Physics and Ion-beam Application (MOE) and Institute of Modern Physics, Fudan University, Shanghai 200443, People's Republic of China.

[h]Also at State Key Laboratory of Nuclear Physics and Technology, Peking University, Beijing 100871, People's Republic of China.

[i]Also at School of Physics and Electronics, Hunan University, Changsha 410082, China.

[j]Also at Guangdong Provincial Key Laboratory of Nuclear Science, Institute of Quantum Matter, South China Normal University, Guangzhou 510006, China.

[k]Also at MOE Frontiers Science Center for Rare Isotopes, Lanzhou University, Lanzhou 730000, People's Republic of China.

[l]Also at Lanzhou Center for Theoretical Physics, Lanzhou University, Lanzhou 730000, People's Republic of China.

[m]Also at the Department of Mathematical Sciences, IBA, Karachi 75270, Pakistan.

[n]Also at Ecole Polytechnique Federale de Lausanne (EPFL), CH-1015 Lausanne, Switzerland.

[o]Also at Helmholtz Institute Mainz, Staudinger Weg 18, D-55099 Mainz, Germany.

[p]Also at School of Physics, Beihang University, Beijing 100191, China.